



Three-Dimensional Distribution of Platinum Group Minerals in Natural MSS-ISS Ores From the Norilsk One Deposit, Russia

J. Sittner^{1,2*}, V. Brovchenko³, A. Siddique², F. Buyse², M. Boone⁴, A.D. Renno¹, V. Cnudde^{2,5}, M. Merkulova² and S.F. Sluzhenikin³

¹Helmholtz-Zentrum Dresden-Rossendorf, Helmholtz Institute Freiberg for Resource Technology, Freiberg, Germany, ²ProGRess-UGCT, Geology Department, Ghent University, Ghent, Belgium, ³Institute of Geology of Ore Deposits Mineralogy, Petrography, and Geochemistry, Russian Academy of Sciences, Moscow, Russia, ⁴TESCAN XRE, Ghent, Belgium, ⁵Department of Earth Sciences, Utrecht University, Utrecht, Netherlands

OPEN ACCESS

Edited by:

Massimo Chiaradia,
Université de Genève, Switzerland

Reviewed by:

Ariadni Georlatou,
GNS Science, New Zealand
Eduardo Mansur,
Geological Survey of Norway, Norway

*Correspondence:

J. Sittner
j.sittner@hzdr.de
Jonathan.sittner@Ugent.be

Specialty section:

This article was submitted to
Economic Geology,
a section of the journal
Frontiers in Earth Science

Received: 23 January 2022

Accepted: 07 March 2022

Published: 23 March 2022

Citation:

Sittner J, Brovchenko V, Siddique A,
Buyse F, Boone M, Renno AD,
Cnudde V, Merkulova M and
Sluzhenikin SF (2022) Three-
Dimensional Distribution of Platinum
Group Minerals in Natural MSS-ISS
Ores From the Norilsk One
Deposit, Russia.
Front. Earth Sci. 10:860751.
doi: 10.3389/feart.2022.860751

The Mt. Rudnaya MSS-ISS (monosulfide and intermediate solid solution) fine-grained ores from a NE termination of Norilsk 1 deposit were analyzed using a combination of X-ray computed micro tomography, spectral X-ray computed micro tomography and scanning electron microscopy to achieve both, 2D and 3D data. The ores consist of ISS composed of tiny lamellar intergrowths of cubanite and chalcopyrite solid solutions, which form up to 4-mm distinct globules surrounded by an ISS-MSS matrix. Our X-ray computed micro tomography results may provide 3D textural evidence of a possible natural sulfide-sulfide liquid immiscibility between Cu-rich and Cu-poor sulfide liquids that occurred before MSS and ISS were crystallized. The platinum group minerals (PGM) distribution shows that 20.6 vol% of all PGM occur in the ISS-MSS matrix and 79.4 vol% in the ISS globules. We suggest that this distributional behavior is due to the fact that the platinum group elements (PGE) cannot be dissolved in ISS, which led to the formation of the large PGM grains, which are up to 120 μm on their longest axis. The initial enrichment of ISS in PGE was controlled by differences in the partition coefficients of platinum and palladium between Cu-poor and Cu-rich liquids.

Keywords: Norilsk, platinum group minerals, X-ray computed tomography, spectral X-ray computed tomography, 3D imaging, SEM-EDS

INTRODUCTION

Platinum group minerals (PGM) are characterized by the presence of platinum group elements (PGE: Ru, Os, Ir, Rh, Pt, Pd) and can be found in different geological settings such as layered intrusions (Kinloch, 1982; McLaren and De Villiers, 1982; Voordouw et al., 2010), ophiolites (Augé, 1988; Economou-Eliopoulos et al., 2017), komatiites (Fiorentini et al., 2004; Locmelis et al., 2009), or magmatic sulfide deposits (Evstigneeva and Genkin, 1983; Genkin and Evstigneeva, 1986; Sluzhenikin et al., 2020). Among the most famous deposits, characterized by a variety of different PGM, is the Norilsk-Talnakh camp, which hosts several Cu-Ni-PGE deposits. Cu-Ni-PGE deposits in general can be very variable in their PGE contents compared to other deposits such as layered mafic intrusions (O'Driscoll and González-Jiménez, 2016). The Norilsk-Talnakh camp though is highly enriched in PGEs and not only is one of the largest Ni sources, but is also an

important Pd producer (Naldrett, 1999; Rao and Reddi, 2000; O'Driscoll and González-Jiménez, 2016). According to recent estimations, the deposits produced 8.3 million tons of Ni, 16.3 million tons of Cu, and 178 million ounces of PGE since the start of mining (Barnes et al., 2020a). Although, since their discovery in 1920, there have been numerous studies on these deposits, a significant part of the geology and genesis is yet to be understood (Kotulsky, 1946; Godlevsky, 1959; Dodin and Batuev, 1971; Genkin et al., 1981; Distler et al., 1988; Duzhikov et al., 1988; Naldrett et al., 1992; Dyuzhikov, 2004; Likhachev, 2006; Arndt, 2011; Ryabov et al., 2014; Duran et al., 2017; Krivolutskaia et al., 2018; Barnes et al., 2019, 2020a; Mansur et al., 2020; Sluzhenikin et al., 2020).

One interesting factor on the genesis and the future mining of Cu-Ni-PGE deposits is the distribution of PGE within the deposit. They can build distinct minerals in the form of PGM and can also be found in different sulfides such as pyrrhotite, pentlandite, or pyrite in various forms including, as nano-inclusions, homogeneous solid solutions, patchy disordered solid solutions, or as ordered solid solutions with a superlattice (Dare et al., 2010; Junge et al., 2015). The distribution of PGE within a deposit depends on various factors during ore formation some of which are fractionation and segregation (Li et al., 1992; Naldrett et al., 1999), hydrothermal redistribution (Farrow and Watkinson, 1997; Barnes et al., 2006; Godel and Barnes, 2008), desulfurization due to interaction of fluids and host rocks (Li and Ripley, 2006; Prichard et al., 2013), or exsolution (Wirth et al., 2013; Junge et al., 2015; Mansur and Barnes, 2020).

The characterization of PGM and their distribution in ores is often performed using different two-dimensional (2D) imaging techniques such as scanning electron microscopy (SEM) in combination with energy dispersive X-ray spectrometry (EDS). However, this comes with some problems regarding mineral shape and the measured sample volume. Therefore, three-dimensional (3D) methods such as X-ray computed microtomography (micro-CT) are becoming more popular for a more representative 3D characterization of complex materials such as natural rocks and ores (Ketcham and Carlson, 2001; Cnudde et al., 2006; Cnudde and Boone, 2013; Reyes et al., 2017). Micro-CT provides exceptional 3D data of internal structures but a major drawback is the lack of chemical information as it only provides greyscale images. However, a relatively new approach to achieve both 3D spatial information and chemical data from X-ray micro-CT scans is a combination with photon-counting detectors (PCD), which provide spectral information (Taguchi et al., 2007; Wang et al., 2011; Boone et al., 2014; Egan et al., 2015; Sittner et al., 2020, 2021; Van Assche et al., 2021). This technique is generally referred to as hyperspectral CT (Chen et al., 2017; Wu et al., 2017; Fang et al., 2019), multispectral CT (Kheirabadi et al., 2017; Devadithya and Castañón, 2021), or spectral CT (sp-CT) (Roessl et al., 2011; Potop et al., 2014; Liu et al., 2015; Sittner et al., 2020; Godinho et al., 2021). The latter term, spectral CT or sp-CT will be further used in this work.

The aim of this work is to analyze the 3-dimensional distribution of the PGM in different sulfide types in the massive ore offshoots of Mt. Rudnaya. Based on the above, we

use SEM-EDS and X-ray micro-CT integrated with sp-CT to obtain non-destructive chemical data of complex ore systems.

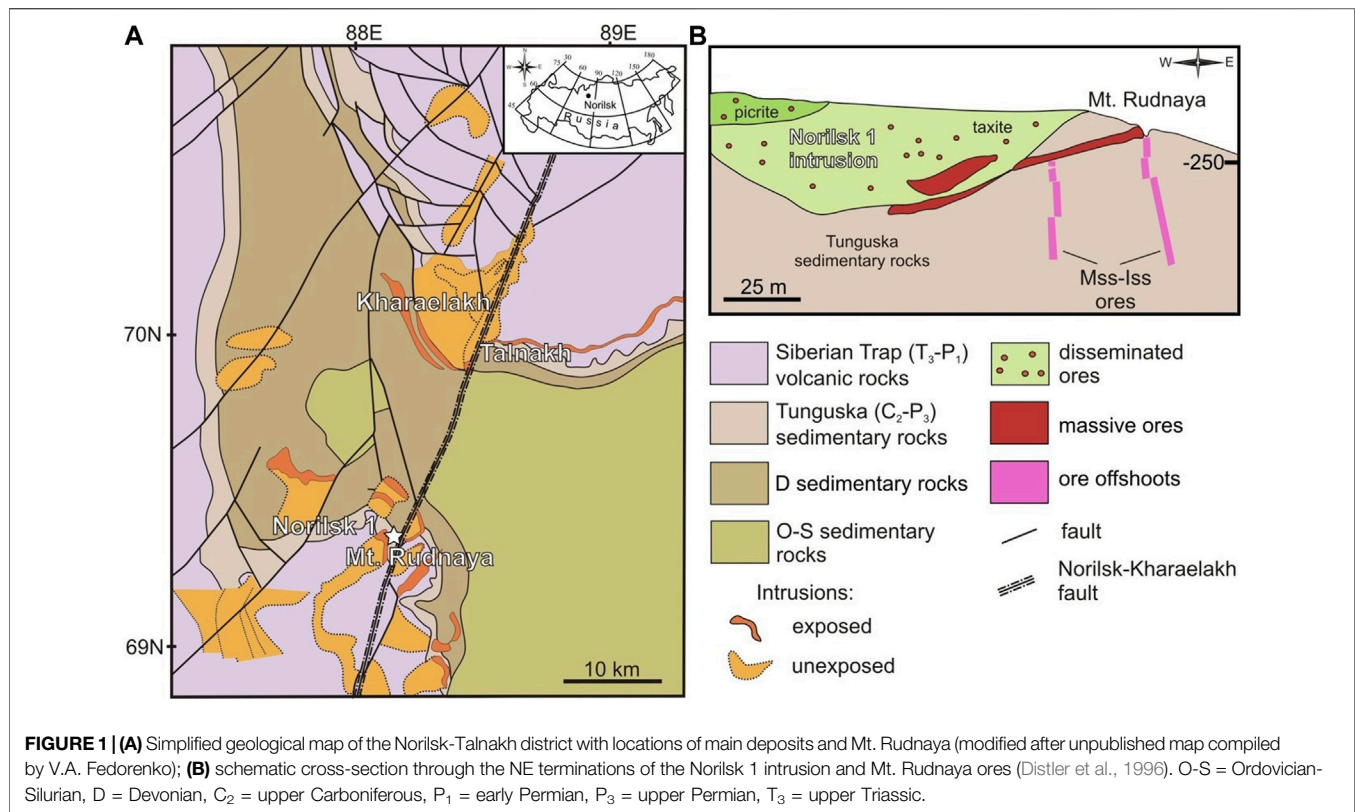
GEOLOGICAL BACKGROUND

Geology and Petrology

The Norilsk-Talnakh district located in the northwestern segment of the East Siberian platform in Russia, is a part of the Siberian Large Igneous Province (LIP). The Siberian LIP represents Earth's largest ultramafic-mafic magmatic event that occurred ~250 Myr ago at the Permo-Triassic boundary (Burgess and Bowring, 2015) leading to the formation of tuffs, lavas, and subvolcanic intrusions. The Norilsk-Talnakh district is covered by 3.5-km-thick Siberian Trap basalts overlying the ~5-km-thick Paleozoic sedimentary rocks hosting hypabyssal ultramafic-mafic intrusions. The Siberian Trap basalt sequence consists of 11 formations deriving from three magmatic stages (Dyuzhikov et al., 1988). According to Latyshev et al. (2020), the formation of Norilsk-Talnakh intrusions occurred contemporaneously with the latest Siberian Trap basalt sequences and can be assigned to the third magmatic stage.

The ore-bearing Norilsk-Talnakh intrusions namely Norilsk 1, Talnakh, and Kharaelakh are situated along the Norilsk-Kharaelakh fault (Figure 1A). The Norilsk 1 differentiated intrusion outcropping west of the Norilsk-Kharaelakh fault, is characterized by a chonolith-like morphology (Yakubchuk and Nikishin, 2004). It is mostly hosted by the Siberian Trap basalt sequences of the second magmatic stage and by sedimentary rocks of the Tunguska series (C₂-P₃) (Dyuzhikov et al., 1988). The internal structure of the Norilsk 1 intrusion is similar to the other ore-bearing differentiated intrusions of the Norilsk-Talnakh district and comprises the Upper Gabbroic series, Main Layered Series, and Lower Gabbroic Series (Dyuzhikov et al., 1988). The Norilsk 1 intrusion is composed of a variety of intrusive rocks such as leucogabbro, gabbrodiorite, olivine-free (0 modal % of olivine), olivine-bearing (0–10% of olivine), olivine (10–20% of olivine), and picritic (20–60% of olivine) gabbrodolerites, taxitic and contact gabbrodolerites. Gabbrodolerite is a specific Norilsk-Talnakh' term for gabbro with fine-grained dolerite texture. The petrographic and lithologic features of the Norilsk 1 intrusion have been described in detail in numerous studies (Dyuzhikov et al., 1988; Naldrett et al., 1992; Ryabov et al., 2014; Sluzhenikin et al., 2020 among many others) and will not be discussed here. The main subjects of this work are the Cu-Ni-PGE ores, which are associated with both intrusive and host rocks and are morphologically divided into massive, disseminated, and veinlet-disseminated ores (Dodin et al., 1971; Dyuzhikov et al., 1988).

The massive ores mostly occur in the lower exo- and endo-contact of intrusions (Dyuzhikov et al., 1988). They form extensive orebodies (up to 2.4 km³), small-scale lenses, and thin veins, and they are composed of Fe-Ni sulfides such as pyrrhotite and pentlandite and Cu-Fe sulfides such as chalcopyrite, cubanite, and others. Fe-Ni sulfides represent subsolidus transformation products of monosulfide solid solution (MSS). In contrast, Cu-Fe sulfides represent



subsolidus transformation products of the intermediate solid solution (ISS). Both MSS and ISS are subsequently converted at subsolid temperatures to the base metal sulfides (BMS) mentioned above (Craig and Kullerud, 1969; Cabri, 1973). Although subsolidus origin of pentlandite has been proofed by many experiments (e.g., Helmy et al., 2021), an alternative way of pentlandite formation due to peritectic reaction between MSS and Cu-rich liquid can be a plausible origin for Pd-rich primary magmatic contact pentlandite (Distler et al., 1977; Kosyakov et al., 2001; Kitakaze et al., 2016; Mansur et al., 2019; Barnes et al., 2020b; Brovchenko et al., 2020).

The disseminated ores are the most common ore type in the Norilsk-Talnakh camp (Dyuzhikov et al., 1988). They occur in taxitic, picritic, and contact gabbrodolerites, and form a large number of different subtypes in some cases depending on the host rock characteristics. For example, one characteristic of the high magnesium “picritic gabbrodolerite” of the Main Layered Series is the widespread occurrence of globular sulfide ores, also called blebby ores, representing an accumulation of sulfide liquid droplets. The bottom of the droplets consists of pyrrhotite and pentlandite and the top consists of chalcopyrite and/or cubanite. This zonation of droplets demonstrates the fractional crystallization of the trapped sulfide liquid inducing the internal separation into Cu-poor Mss and Cu-rich Iss components (Barnes et al., 2006). The Norilsk-Talnakh globular ores were studied by several analytical methods (Czamanske et al., 1992; Barnes et al., 2006), including high-resolution X-ray micro-CT (Le Vaillant et al., 2017; Barnes et al., 2019, 2020a). The results obtained by X-ray micro-CT especially

in combination with 2D micro-X-ray fluorescence mapping provided important insights about sulfide-silicate micro-textural relations, which helped scientists to further understand the origin of the globular ores (Barnes et al., 2017). For instance, the role of volatiles in sulfide transport was proved to be significant (Mungall et al., 2015; Le Vaillant et al., 2017; Yao and Mungall, 2020).

The massive ores also show signs of separation of initial sulfide liquids. For example, Cu-poor pyrrhotite ores usually form the bottom of sulfide orebodies, while Cu-rich ores occur as massive ores, veins, and breccias at the top of orebodies or around them (Dyuzhikov et al., 1988; Naldrett, 2004; Barnes and Lightfoot, 2005; Duran et al., 2017).

In the Norilsk-Talnakh sulfide ores Pd, Pt, Rh, Ru, Ir, and Os usually occur in form of distinct minerals such as PGE alloys, intermetallic alloys with Fe, Ni, Cu, Pb, TABS (Te, As, Bi, Sb, Sn), and PGE sulfides (Genkin and Evstigneeva, 1986). Pyrrhotite massive ores at Norilsk-Talnakh deposits are the most enriched in IPGE (Ru, Os, Ir) (Miroshnikova, 2017) and as shown by Tolstykh et al. (2022) can contain up to 12.25 ppm of Ir, Ru, Rh in total. This type of ores represents the first Cu-poor sulfide liquid which mostly crystallized MSS. In contrast, ores that are most enriched in Pt and Pd are believed to be formed from an evolved Cu-rich sulfide liquid and have been noted to occur in the upper horizons of the layered intrusions (Duran et al., 2017; Sluzhenikin et al., 2020) or at the external offshoots (Brovchenko et al., 2020).

One of those offshoots is located on the northern cape of Mt. Rudnaya in the NE termination of the Norilsk 1 deposit

(**Figure 1B**). Mt. Rudnaya offshoots were tracked down from their connection with the massive pyrrhotite ore body and occur as two 0.5 m - thick veins up to 90 m in length hosted by Tunguska sandstone and mudstone with coal beds. The deepest terminations of these veins were composed of fine-grained ores of primary magmatic MSS, ISS, and pentlandite and were extremely enriched in PGE with an average concentration up to 350 ppm. The mineralogy and petrology of the MSS-ISS ores have been described in detail (Distler et al., 1996; Brovchenko et al., 2020). A specific texture of these ores is a spreading of up to 4 mm globular ISS segregations among an MSS-ISS matrix with pentlandite grains at its contact. PGM are mostly observed in ISS globules and may form euhedral or skeletal grains from nanometer size to 100 μm sometimes in porous intimate intergrowths with each other.

Sulfide Liquid Evolution, PGE, and PGM

The characteristics of sulfide liquids are mainly ruled by the process of fractional crystallization (Ebel and Naldrett, 1996). Fractional crystallization promotes a constant enrichment of newly formed phases in elements compatible to them (Li et al., 1992). The compatibility of different elements into MSS, ISS, and sulfide liquids is described by the partition coefficients. Due to fractional crystallization IPGE (Ru, Os, Ir) and Rh become enriched in initial unfractionated Cu-poor sulfide liquid, whereas residual Cu-rich liquid accumulates Pd, Pt, Au, Ag, and TABS. This was observed in several experimental studies (Distler et al., 1977; Fleet and Stone, 1991; Fleet et al., 1993; Ballhaus et al., 2001; Mungall et al., 2005; Cafagna, 2015; Liu and Brenan, 2015; Sinyakova et al., 2016) as well as in some natural occurring ore deposits (Ebel and Naldrett, 1996; Naldrett, 2004; Dare et al., 2010; Duran et al., 2017).

As for Norilsk-Talnakh massive ores, the X-ray micro-CT results showed that Cu-rich ISS cumulates contain remarkably more PGE and TABS minerals than Cu-poor MSS cumulate ores (Duran et al., 2017). A separation of the Cu-rich residual liquid fractionated from the initial Cu-poor MSS dominated cumulate, is commonly believed to be caused by earlier crystallization of MSS at 950°C (Helmy et al., 2021) and the higher ability of Cu-rich sulfide liquid to wet silicates (Ebel and Naldrett, 1996; Barnes et al., 2017). After separation, the Cu-rich fractionated sulfide liquid crystallizes ISS at 700°C (Helmy et al., 2021). In contrast Pd, Pt, Au, Ag, and TABS remain in residual liquid eventually forming small portions of evolved liquid extremely enriched in these elements (Dare et al., 2010; Holwell and McDonald, 2010; Tomkins, 2010; Liu and Brenan, 2015). As a result of the crystallization of this late-stage liquid, PGM are formed. However not all PGM form at the late stage of the evolution of sulfide liquid. In magmatic sulfide deposits, it is believed that isoferroplatinum, cooperite, and laurite are the earliest PGM forming at high temperatures (Genkin and Evstigneeva, 1986; Yudovskaya et al., 2017).

Mt. Rudnaya MSS-ISS ores were formed due to downward penetration of the fractionated Cu-Ni-PGE rich sulfide melt into subvertical fractures (Brovchenko et al., 2020). According to their model, MSS₁ and its eutectic assemblage with early formed PGMs

were crystallized from the first cumulates of sulfide liquid (L₁). The residual sulfide liquid (L₂) became more enriched in PGEs due to fractional crystallization, and eventually crystallized ISS₂ from globules which captured early formed PGMs. The ISS₃ and MSS_{2,3} from ISS-MSS matrix were crystallized from the last sulfide liquid (L₃), while pentlandite was formed by peritectic reaction between MSS and the residual sulfide liquid. An exchanging between different generations of MSS, ISS and the residual sulfide liquids caused the directional distribution of Pd in the contact pentlandite grains and the wide variations of trace and major components concentrations in sulfide solid solution. Distler et al. (1996) suggested that ISS globules from Mt. Rudnaya ores are the result of a local sulfide-sulfide immiscibility in sulfide liquid, whereas Brovchenko et al. (2020) proposed that the rounded form of ISS globules occurred due to swirling motion of the sinking sulfide liquid. The PGMs distributional behavior in Mt. Rudnaya MSS-ISS ores have not been discussed earlier but its detailed examination can resolve remaining questions about Mt. Rudnaya MSS-ISS ores formation.

MATERIALS AND METHODS

Sample Material

Twelve samples of the fine-grained ores were used for this study and were selected from a collection of the Mt. Rudnaya underground mine 2/4 (also known as Morozov mine), which are described in (Distler et al., 1996; Brovchenko et al., 2020). The samples are embedded in two 2 × 5 mm polished blocks of epoxy (RM1 and RM2) (**Figures 2A,B**). Mt. Rudnaya's fine-grained massive ores are composed of ISS (consisting of cubanite and chalcopyrite solid solutions lamellar intergrowths), which forms globules up to 4 mm, surrounded by inner bands of pentlandite grains and external rims of MSS grains (**Figure 2E**) (samples RM1.1, RM1.10, RM1.11, RM1.29, RM1.30, RM1.31), sometimes without pentlandite (samples RM1.12) (**Figures 2C,F**). The second type of textures are globules of MSS or MSS-ISS surrounded by an ISS-MSS matrix (samples RM1.2, RM2.6, RM1.11) (**Figure 2D**). According to electron probe micro analysis (EPMA) data presented in Brovchenko et al. (2020), the observed phases have a nonstoichiometric composition and correspond to experimentally produced MSS and ISS (Fleet et al., 1993; Raghavan, 2004; Helmy et al., 2007). Mt. Rudnaya ISS-MSS ores contain numerous grains of platinum and palladium minerals and Au-Ag alloys. The most common Pt mineral observed in MSS-ISS Mt. Rudnaya ores is tetraferroplatinum (PtFe). It is usually surrounded by a 1 μm rim of Pt-Fe alloys with Pt₂Fe and Pt₃Fe₂ compositions. Cooperite (PtS) is less abundant and forms intimate intergrowths with Pt-Fe alloys and Pd minerals. Palladium not only occurs in individual minerals such as Pd-rich rustenburgite (Pt₃Sn) and Pt-rich atokite (Pd₃Sn) but also in enriched pentlandite (up to 4.62 wt%). Platinum occurs only in PGM. Porous intergrowth is a common feature of palladium minerals, but they mostly form individual grains up to 10 μm at the edge of PGM aggregates.

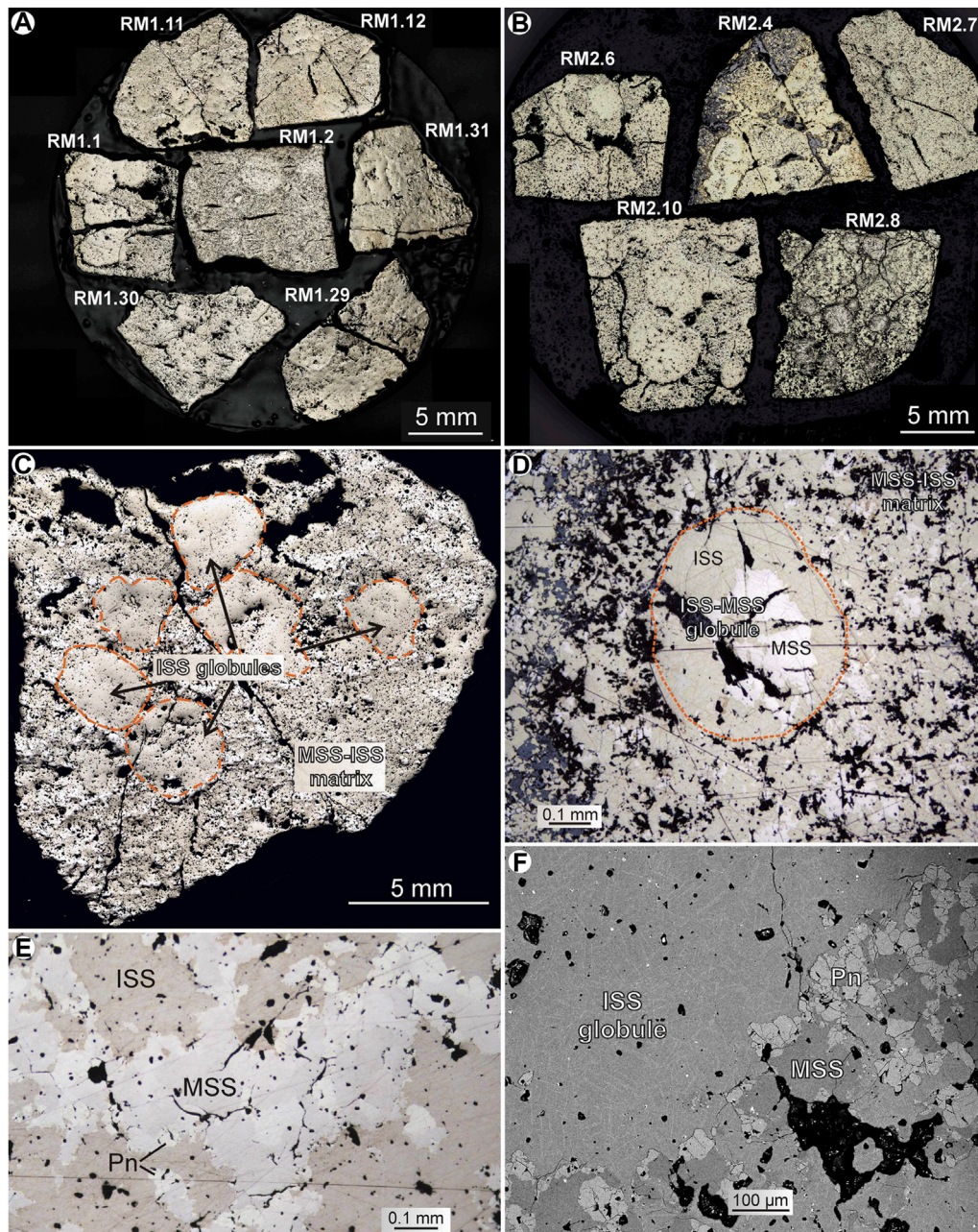


FIGURE 2 | Microphotographs of investigated samples; **(A)**: sample RM1; **(B)**: sample RM2; **(C,D)**: a typical texture of samples - ISS globules in an MSS-ISS matrix and ISS-MSS globule in MSS-ISS matrix (c—RM1.1, d—RM1.2) (c—RM1.1, d—RM1.30). **(E)**: MSS-ISS matrix with pentlandite grains at the contact between MSS and ISS (RM1.29). **(F)**: an edge of the ISS globule in BSE (RM1.29); Pn—pentlandite.

X-ray Micro-CT and Sp-CT

X-ray micro-CT is a non-destructive 3-dimensional imaging analysis technique, which is used for the investigation of internal structures (Cnudde and Boone, 2013). It is based on the different X-ray absorption behavior of materials within a sample, which create contrast in the resulting grayscale image (Ketcham and Carlson, 2001). In the past years, the technique proved its applications in different disciplines of geoscience including the characterization of ores in 3D (Godel et al.,

2010; Chetty et al., 2012; Godel, 2013; Yang et al., 2014; Reyes et al., 2017; Yang et al., 2017; Barnes et al., 2019). As micro-CT cannot provide chemical information, prior knowledge about the sample composition is needed on which different absorption coefficients for the individual minerals can be calculated (Cnudde and Boone, 2013). Therefore, it is often used in combination with other methods such as SEM-EDS when characterizing geological materials (Godel et al., 2010; Chetty et al., 2012; De Boever et al., 2015; Reyes et al., 2017).

In this work we use sp-CT in combination with micro-CT as an additional method to provide chemical information. The basis of sp-CT is the detection of the X-rays after their interaction with the sample. For the detection, different PCD materials can be used such as CdTe or CdZnTe (Takahashi and Watanabe, 2001). The detected spectrum contains different features such as absorption edges that are element specific. Based on the energy position of these edges elements can be identified (Sittner et al., 2020, 2021).

For all X-ray computed tomography scans presented in this study, we used the TESCAN CoreTOM micro-CT scanner (at the Helmholtz Institute Freiberg for Resource Technology in Germany and at TESCAN-XRE in Ghent, Belgium), which is optimized for a high-resolution and large field of view imaging. The standard imaging detector is an amorphous Si flat panel detector with a surface of 428.4 by 428.4 mm² and 2,850 by 2,850 pixels. Furthermore, the system is equipped with an additional photon-counting line sensor, the TESCAN PolyDet, which can automatically slide in front of the standard detector (Sittner et al., 2020). It is a CdTe semiconductor X-ray detector with a sensor width of 307 mm with 0.8 by 0.8 mm square pixels. The direct detection sensor has an energy range from 20 up to 160 keV and can discriminate up to 128 energy bins for each of the 387 pixels that represent the horizontal field of view. In particular, the K-edge of elements from Cd up to U can be detected with this detector (Sittner et al., 2020). The different X-ray micro-CT scans were reconstructed using Aquila reconstruction (version 1.14) by TESCAN-XRE. The sp-CT scans were reconstructed using the spectral reconstruction module in Aquila reconstruction with a fan beam reconstruction, a ring filter, and a spot filter correction.

As a first step of the workflow, the samples were measured using standard X-ray micro-CT. Therefore, an overview scan of both individual samples (RM1 and RM2) was performed with the full sample in the field of view. Afterwards, the same was applied with the sp-CT measurements. As the PCD used in this work is a line sensor, numerous 2D overview planes at different positions of the samples were scanned. With the results of these measurements, specific regions of the samples were selected for further investigation and higher resolution scans with X-ray micro-CT and sp-CT. These regions were selected based on the occurring minerals and features that were observed in the overview scans. As a last step, the samples were scanned with SEM-EDS (see 3.3) for a correlation of the CT measurements. This enables a chemical differentiation of the individual minerals in the samples in addition to the sp-CT.

Samples RM1 and RM2 were initially scanned with a tube voltage of 180 keV, a power of 15 W, and an exposure time of 1.0 s. Moreover, a voxel size of 9.2 μm was achieved. Afterwards, specific areas of the samples were scanned in detail in a so-called volume of interest (VOI) scan. A tube voltage of 180 keV, a power of 15 W, and an exposure time of 5.0 s were used to achieve a voxel size of 5.3 μm.

Sp-CT scans of the complete samples were done at a tube voltage of 160 keV, a power of 30 W, and an exposure time of 1.0 s. Moreover, an average of 20 spectra per angle was used to reduce noise. For the same field of view, the voxel size of the sp-CT scans is higher compared to the X-ray micro-CT resulting in a lower resolution of the sp-CT images. This is caused by the lesser amount of pixels

available in the PolyDet compared to the standard detector, which results in a voxel size that is 7.3 times higher (Sittner et al., 2020; Godinho et al., 2021). For these scans, the voxel size was 68.1 μm. No filter was used for these scans as it influences the detected spectrum. Moreover, VOI scans were performed using sp-CT to have a better resolution for certain regions. Therefore, a tube voltage of 160 keV, a power of 25 W, and an exposure time of 1.0 s were used with 20 averages. With these settings, we were able to achieve voxel sizes of 44.2 and 28.2 μm respectively. All spectral CT scans were done with 600 projections per 360°. **Table 1** summarizes the scanning conditions of all sp-CT and X-ray micro-CT scans.

SEM-EDS

SEM-EDS measurements of the samples were performed using the MIRA3 TESCAN scanning electron microscope equipped with a field emission gun (at Ghent University, Belgium). Apart from the backscattered electron (BSE) detector, the system is equipped with an energy dispersive X-ray silicon drift detector (EDAX Element 30) for EDS measurements. The data analysis was done in the software TESCAN TIMA (version 1.7.0).

A carbon coating was applied to both samples before scanning to inhibit charging. The samples were scanned in liberation analysis mode with the high-resolution acquisition mode (Hrstka et al., 2018). A pixel spacing of 5 microns was used with 1,000 counts per spectrum per point. Before each scan, the system was calibrated by using a platinum and a manganese standard. Both scans were done at a working distance of 15 mm and with an acceleration voltage of 25 kV, a probe current of 22.22 nA, and a spot size of 79.72 nm.

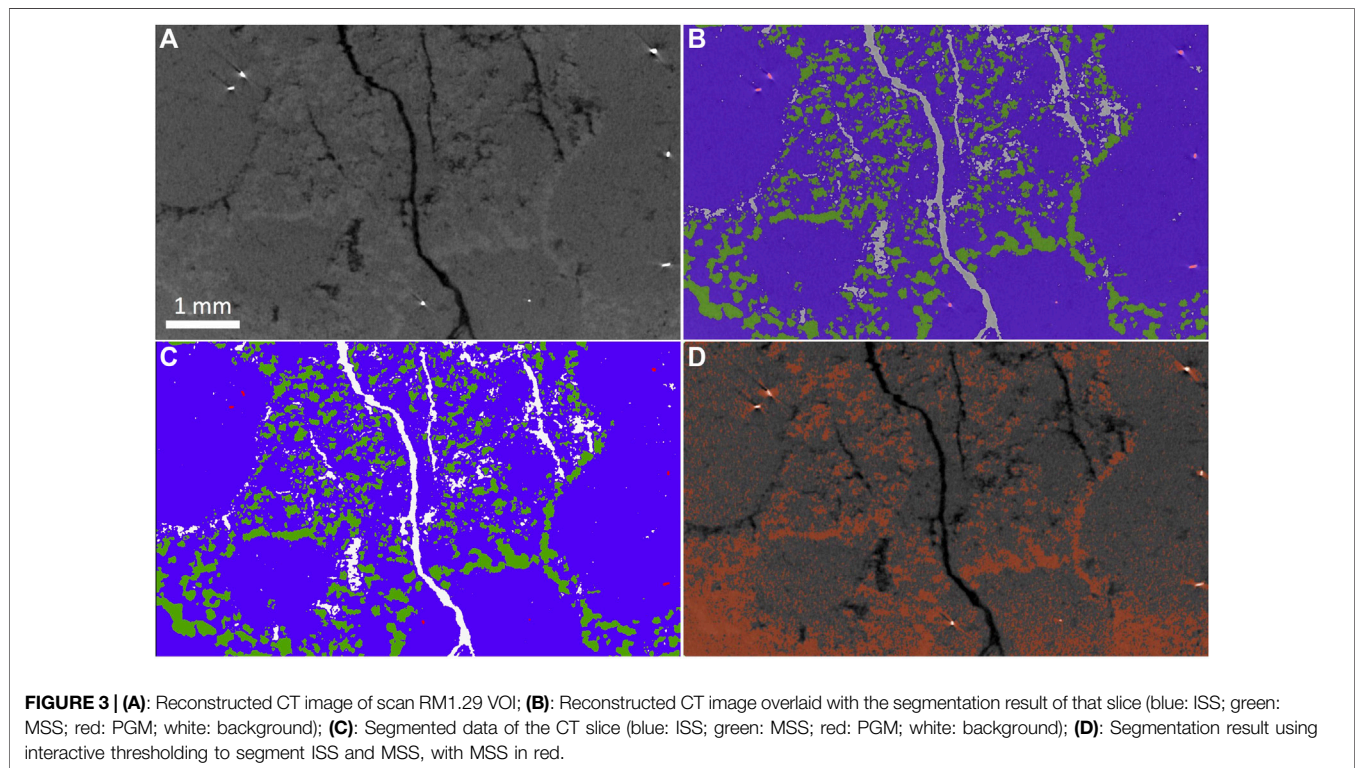
To correct for the stereological bias of the 2-dimensional measurement, a stereological correction was applied to the data by using the program CSD Corrections 1.60 (Higgins, 2000). It was assumed that the grain shape of the PGM is spherical and no preferential orientation of the PGM occurs in the studied samples. The 2D length and width measurements were used for stereological correction.

Segmentation Workflow

The software Dragonfly (version 2021.1) by ORS was used for the segmentation of the micro-CT data. It features different machine learning and deep learning algorithms that can be used for segmenting different phases (Piche et al., 2017; Makovetsky et al., 2018; Badran et al., 2020; Reznikov et al., 2020). The segmentation of different mineral phases solely based on the greyscale values is often challenging due to the artifacts caused by micro-CT and complex mineralogical distribution of fine and dense minerals. However, recent advancements in computing powers along with the development of machine and deep learning algorithms to segment phases have made it possible to overcome the micro-CT artifacts for accurate quantification. To achieve precise segmentation, the algorithm needs a training dataset to learn how to make predictions for later calculations, which is often a time-consuming step. For this purpose, single or multiple 2D slices of the reconstructed micro-CT volumes are used with labeled voxels belonging to different segmentation classes. These slices are then used for the training as well as validation of the algorithm.

TABLE 1 | Summary of the X-ray micro-CT and sp-CT scanning conditions for the different samples.

| X-ray micro-CT measurement | Tube voltage in keV | Tube power in W | Voxel size in μm | Exposure time in ms | Number of projections | Scanning time in minutes |
|----------------------------|---------------------|-----------------|-----------------------------|---------------------|-----------------------|--------------------------|
| RM1 overview | 180 | 15 | 9.2 | 1,000 | 4,268 | 464 |
| RM2 overview | 180 | 15 | 9.2 | 1,000 | 4,268 | 465 |
| RM1.29 VOI | 180 | 15 | 5.3 | 5,000 | 3,000 | 260 |
| Sp-CT measurement | | | | | | |
| RM1 overview | 160 | 30 | 68.1 | 100 | 600 | 24 |
| RM2 overview | 160 | 30 | 68.1 | 100 | 600 | 24 |
| RM1.29 VOI | 160 | 25 | 44.2 | 100 | 600 | 15 |
| RM2.10 VOI | 160 | 25 | 28.2 | 100 | 600 | 23 |



The segmentation models were trained separately for the overview scans and volume of interest (VOI) scan. In the case of the VOI scan, four segmentation classes consisting of ISS, MSS, PGM, and background were trained. The two overview scans were trained with three classes as the measurement conditions did not allow a more precise subdivision between MSS and ISS. Therefore, the classes sulfides, PGM, and background were segmented for these scans. The classes were manually labelled on the basis of mineralogical knowledge based on the SEM-EDS and sp-CT studies. In this study, three algorithms were trained first with the same training data set: random forest (Breiman, 2001), U-Net (Ronneberger et al., 2015), and sensor3D (Novikov et al., 2019). After the first training, these algorithms were tested on a new slice, which was not part of the training data. Of these three models,

sensor3D showed the most accurate segmentation results. Therefore, for further training with more labelled slices, only the sensor3D model was used. This model was trained several times and after each training, the model was tested on a new slice and wrongly classified phases and voxels were corrected and included in the training data set. In this way, the model was trained until an accurate segmentation was obtained and no further improvements were seen with more training (Figures 3A–C). In the VOI measurement, the model struggled to correct streak artifacts from X-ray micro-CT around the PGM grains even after several training sessions. Therefore, these artifacts were corrected manually. The model successfully segmented the ISS and MSS phases in this scan, which is not possible using simple interactive thresholding as Figure 3D shows.

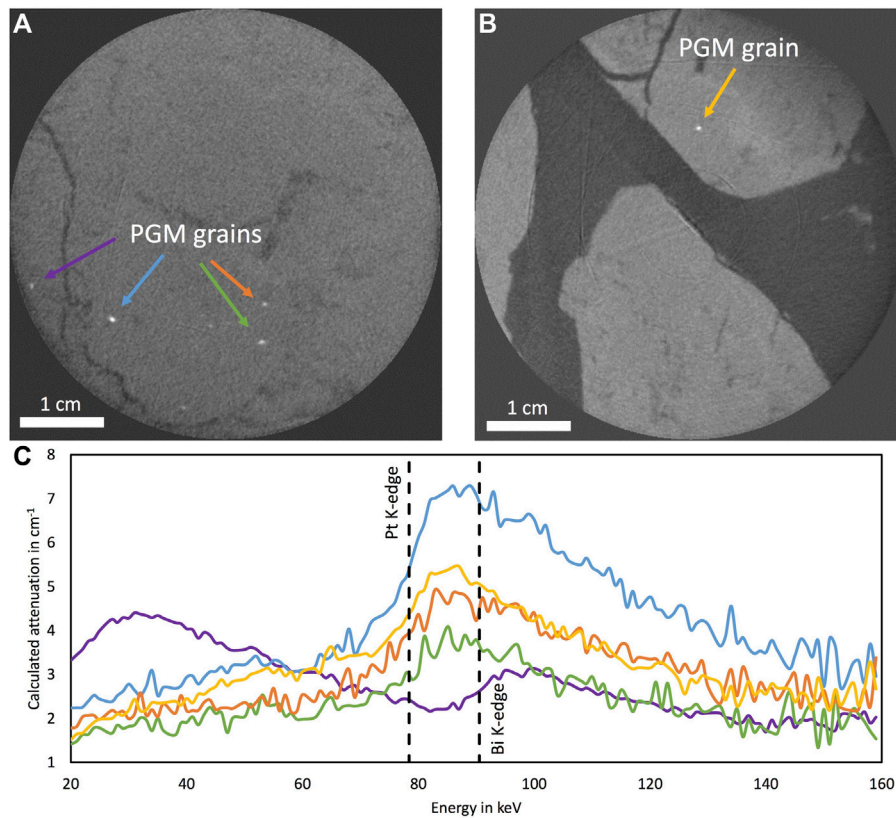


FIGURE 4 | (A): Reconstructed sp-CT scan of sample RM2.10 VOI with different PGM grains; **(B):** Reconstructed sp-CT scan of sample RM1.29 VOI with a PGM grain; **(C):** Spectra of different PGM grains in the samples indicated with different colors and the K-edges of Pt and Bi.

RESULTS

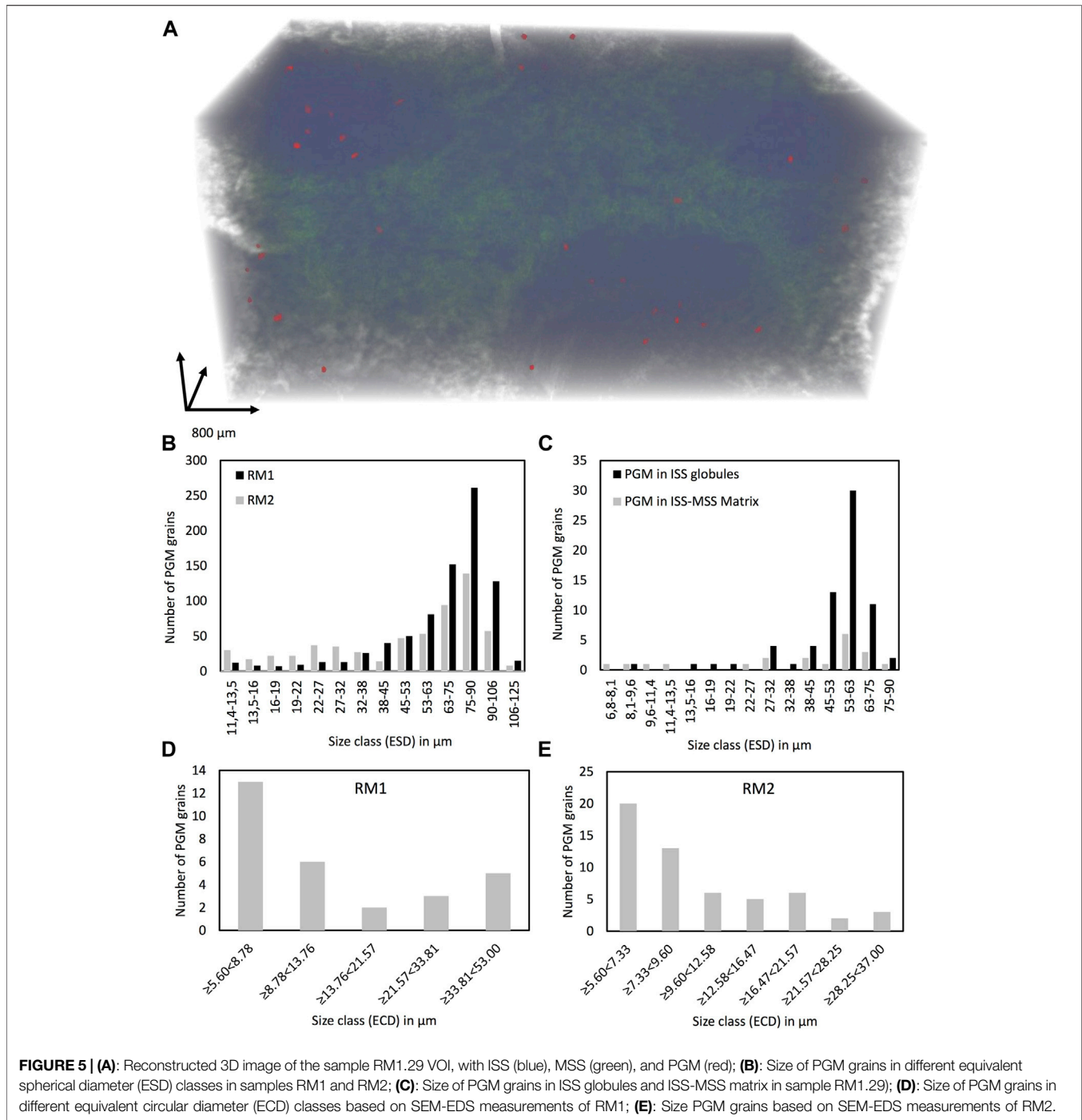
Analysis, Distribution, and Size of PGM

The reconstructed CT images of the samples show high attenuating phases, which can be segmented but not distinguished using X-ray micro-CT (**Figures 4A,B**). With the help of sp-CT, different spectra of these phases can be extracted. The majority of the analyzed grains show K-edges at ~ 78 keV which corresponds with the K-edge energy of Pt at 78.4 keV (Chantler, 2001) (**Figure 4C**). Moreover, one grain shows a K-edge at ~ 90 keV that can be assigned to the K-edge energy of Bi at 90.5 keV (Chantler, 2001). A more detailed determination of the PGM is not possible using sp-CT as no other K-edge was detected. Nevertheless, it enables a first and quick identification of the PGM within the 3D volume, without any destruction of the samples. The SEM-EDS measurements confirm the sp-CT results and further show that most of the PGM are Pt-Fe alloys such as tetraferroplatinum (PtFe), Pt₂Fe, and Pt₃Fe₂. Moreover, platinum group minerals such as cooperite (PtS) and Pt-Sn minerals like rustenburgite (Pt₃Sn), and Pt-rich atokite (Pd₃Sn) are present in the samples but usually occur less frequently. Based on the EDS spectrum the Bi-mineral that was detected with spectral-CT is probably sobolevskite (PdBi) in intergrowth with atokite (Pd₃Sn).

The K-edges of Sn (29.2 keV) and Pd (24.4 keV) though were not detected using sp-CT. This is probably caused by the small grain size in the intergrowth and the low resolution of the sp-CT scan. With a smaller sample size, the resolution could be increased and the K-edges of Sn and Pd could be detected. In contrast, the K-edges of Fe and S are not in the spectral range of the PCD we used for the sp-CT measurements and therefore, are not detectable.

The SEM-EDS results show that the PGM are commonly distributed in the ISS globules that occur in both samples. The 3D data confirm this, as shown in **Figure 5A**. It illustrates a 3D image of the VOI scan of RM1.29 with the segmented phases MSS, ISS, and PGM. The fine-grained structure of the ore makes the illustration of the different classes difficult as they consist of numerous small phases. Nevertheless, the ISS globules are clearly visible in the 3D image. The majority of the PGM occur in these globules but few grains are also found in the ISS-MSS matrix. In total 20.6 vol% of the PGM occur in the ISS-MSS matrix and 79.4 vol% in the ISS globules. This was calculated by manual selection of the PGM in the sample.

For a better vitalization the grain size distribution is calculated for the PGM (**Figure 5B**) with different size classes based on the

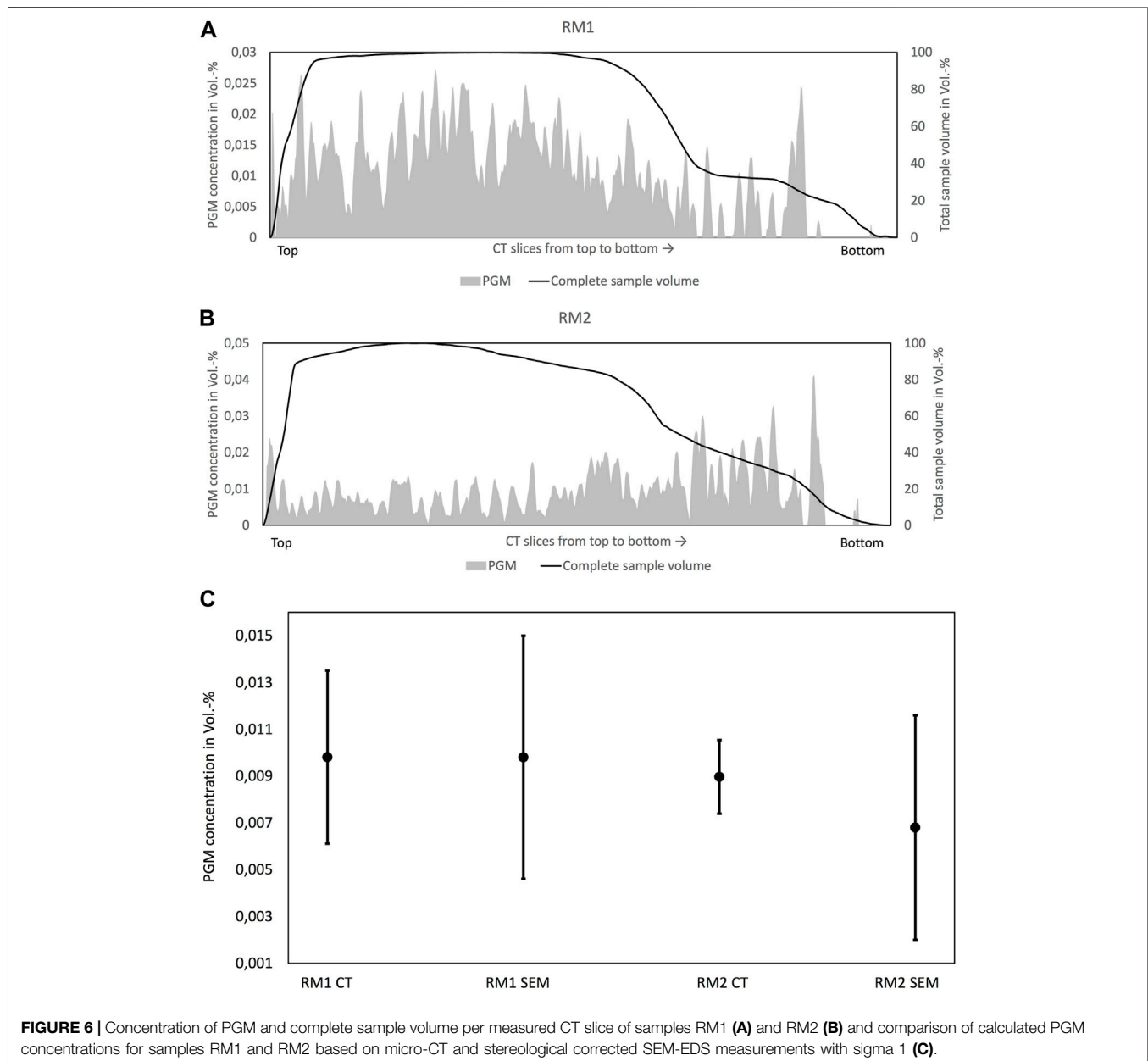


equivalent spherical diameter (ESD), which is described by the equation.

$$ESD = \sqrt[3]{\frac{6 \times \text{volume}}{\pi}}$$

The grain size distribution shows that the PGM sizes range from 11.4 to 125.0 μm in the samples. The minimum grain size is limited by the voxel size which was used for the overview scans as

no PGM grain below this size can be segmented. Most of the PGM occur in the 75–90 μm size class in both samples. Furthermore, sample RM2 is characterized by more small-sized PGM grains in classes below 38 μm . In contrast, sample RM1 shows larger grains particularly in classes above 53 μm . No interdependence between grain size and chemical composition of the PGM was found. When comparing the grain size distribution of PGM between ISS globules and the ISS-MSS matrix the measured grains show sizes between 6.8 and 90 μm , which is again limited by the voxel size of



the micro-CT scan (Figure 5C). The number of individual PGM in the ISS and ISS-MSS matrix is different, but the grain size distribution is similar. The ISS-MSS matrix shows the smallest grain sizes of PGM compared to the ISS globules.

In comparison to the X-ray CT results, the SEM-EDS measurements show smaller grain sizes for the PGM (Figures 5D,E). Here, the sizes vary between 5.6 and 53.0 μm for sample RM1 and between 5.6 and 37.0 μm for sample RM2.

Two-Dimensional and Three-Dimensional Distribution of PGM

For the investigation of trace phases such as PGM, it is important to measure a large and representative sample volume as their

concentration can change drastically within a small scale. To visualize this the distribution of the PGM in samples RM1 and RM2 is calculated from top to bottom (Figure 6). This calculation is based on the concentration of the phases per reconstructed and segmented CT slice from the overview scan. Therefore, the concentration of PGM was calculated for each single reconstructed CT slice of the samples. In total 681 slices were measured for sample RM1 and 676 slices for sample RM2. As a large part of the CT slices consist of epoxy resin, which is considered as the so-called “background”, the PGM concentration was normalized to the volume of the sample material in the specific slice. Moreover, the complete sample volume was calculated to see its progression within the 3D volume of the epoxy block.

The PGM concentration in the two samples can change significantly from one CT slice to another as **Figures 6A,B** show. The concentration varies from 0 to 0.027 vol% in sample RM1 and from 0 to 0.04 vol% in sample RM2, which can be explained by the PGM distribution, which in turn depends mainly on the ISS. This means that in some 2D slices of the samples no PGM grains were detected at all using X-ray micro-CT compared to others which were overestimating the total amount of PGM.

The comparison of the results measured with X-ray micro-CT and the SEM-EDS show some differences as **Figure 6C** indicates. Sample RM1 shows a concentration of 0.0098 ± 0.0037 vol% based on the micro-CT scans and 0.0098 ± 0.0052 vol% based on the SEM-EDS measurements. They can be considered equal concerning the standard deviation of both measurements. For sample RM2 the concentration of the PGM is 0.0089 ± 0.0015 vol% measured with micro-CT and 0.0068 ± 0.0048 vol% using SEM-EDS. As for sample RM1 the concentrations are also equal in terms of the standard deviation. It is noticeable that the standard deviation is higher for both SEM measurements, which can be explained by the low number of PGM grains detected: 19 for sample RM1 and 29 for sample RM2. Compared to the micro-CT scans 815 PGM grains were found in sample RM1 and 602 in sample RM2. Therefore, the overall number of detected grains is significantly higher in the micro-CT scans due to the differences in scanned volume (Ramsey, 2021).

DISCUSSION

Methodology

Our results show that micro-CT in combination with sp-CT is a good addition to 2D methods such as SEM-EDS as it provides exceptional 3D data and a more representative 3D characterization of different phases such as PGM. In this work, the number of analyzed samples is small and a complete and representative characterization of an ore body would require a significantly higher sampling density. But it shows that 2D methods are susceptible to statistical errors when analyzing trace phases with a limited amount of sample material as in this case. With a combination of 2D and 3D methods as shown in this work, the distribution of mineral phases can be better visualized. Moreover, with additional bulk methods such as X-ray diffraction or X-ray fluorescence, the modal concentrations for different minerals can be calculated and compared with micro-CT and SEM-EDS.

There are other possible methods for the analysis of the 3D distribution of different minerals such as dual beam SEM, which combines a focused ion beam (FIB) and an electron beam (Kubis et al., 2004; Keller et al., 2011; Bultreys et al., 2016). This method allows taking SEM images while the FIB sections the sample material. The images can then be reconstructed into a 3D image. However, the analyzed volume is usually less than 10 μm in x- and y-direction and 2 μm in z-direction, making an analysis of the 3D distribution of PGM in the our samples not possible as this volume is too

small (Bultreys et al., 2016). Other 3D methods such as secondary ion mass spectrometry (SIMS) or atom probe tomography face the same problem of a small scanning volume (Kelly and Miller, 2007; Nygren et al., 2007; Hill et al., 2011). Moreover, all these methods are destructive.

As any other method micro-CT has certain limitations not only when it comes to the resolution of small phases but also for in the analysis of minerals with similar attenuation coefficients. The contrast of the greyscale images in micro-CT depends on different factors such as X-ray energy and attenuation coefficient of a measured sample (Knoll, 2000). Therefore, a differentiation of minerals with almost similar attenuation coefficients is difficult. However, with sp-CT it is possible to analyze the absorption edges making a differentiation of specific minerals possible, as seen in **Figure 4**. Another limitation when it comes to the analysis of small phases such as the PGM using micro-CT is the partial volume effect. As a voxel represents the average value of the attenuation coefficient over its complete volume, features below the voxel size contribute to this value (Ketcham and Carlson, 2001; Cnudde and Boone, 2013). Among other things, this effect influences grain boundaries and can thus lead to errors in the segmentation of the volume. Even with modern machine and deep learning segmentation models, this effect cannot be eliminated, as it originates from the voxelized data itself. But there are different software corrections that can be applied to minimize the effect (Rousset et al., 2007; Godinho et al., 2019). Especially small phases such as the PGM grains in the samples are influenced by this. As the boundary voxels are taken into account for the grain size distribution calculation shown in **Figures 5B,C**, the grain sizes are overestimating the actual sizes.

Sulfide-Sulfide Liquid Immiscibility?

A schematic model introduced by Brovchenko et al. (2020) describes the ISS globules, MSS globules, and ISS-MSS matrix as products of different generations of sulfide liquid which were formed due to the fractional crystallization process. According to their model, the ISS globules are the products of the first Cu-rich liquid crystallization, and the ISS from the ISS-MSS matrix was formed later from the more evolved sulfide liquid. Their model was based on 2D textural and LA-ICP-MS study, whereas 3D micro-CT data reveals textural features of globules more clearly. According to our results, the ISS forms distinct spheres (up to 4 mm in diameter) in major part of samples. Inverse textures that are formed by MSS and MSS-ISS globules are less common and are characterized by lower concentrations of PGMs and pentlandite grains. We suppose that spherical segregation of sulfide liquids with different compositions could be caused by liquid-liquid immiscibility. In that case, we speculate that Cu-rich and Cu-poor liquids separate from each other above liquidus temperature before crystallizing ISS or MSS. Similar to the formation of sulfide globules in silicate melts, due to immiscibility a formation of spherical ISS and MSS globules is very probable.

In contrast with generally accepted fractional crystallization no consensus had been reached on the occurrence of liquid immiscibility in the Fe-Ni-Cu-S system as ore formation process (Distler et al., 1986; Peregoedova, 1998; Ballhaus et al.,

2001; Beswick, 2002, 2020; Gorbachev and Nekrasov, 2004; Brenan et al., 2008). Sulfide-sulfide liquid immiscibility in the Fe-Ni-Cu-S system was first established experimentally by Ballhaus et al. (2001) over the temperature range from 1,275 to 900°C. In metal-rich composition experiments, the immiscible Cu₂S-rich liquid formed zoned droplets with an MSS rim surrounded by a FeS-rich liquid in the matrix (Ballhaus et al., 2001). It had also been mentioned that the proportions of these droplets did not exceed 10 vol% of the total bulk and that Cu and PGE were heterogeneously distributed among the droplets (Ballhaus et al., 2001). However, in an attempt to repeat the results by Ballhaus et al. (2001), no sulfide-sulfide liquid immiscibility was detected (Brenan et al., 2008). A relatively homogeneous ISS-MSS matrix from the experiments of Brenan et al. (2008) showed similarities to the ISS-MSS matrix from the Mt. Rudnaya ores. The separation of sulfide liquid into Fe- and Ni-enriched liquid of MSS-like composition and Cu- and Pt-rich liquid of chalcopyrite- and bornite-like composition was reported in Gorbachev and Nekrasov, (2004) experiments at 1,400–1,250°C and 3.5 GPa. ISS-MSS globules (**Figure 2D**) from Mt. Rudnaya MSS-ISS ores have a similar zonation with the products of Gorbachev and Nekrasov, (2004) experiments where MSS occupies center of globule and ISS occurs around the MSS.

The sulfide-sulfide liquid immiscibility was proposed as the main mechanism of separation of Cu-rich and Cu-poor sulfide liquids which causes zoning in sulfide composition either in sulfide droplets from Norilsk-Talnakh deposits (Distler et al., 1986; Gorbachev and Nekrasov, 2004; Gorbachev and Nekrasov, 2004) and Froot deposit at Sudbury (Fleet, 1977), or in McCreedy West deposit at Sudbury (Beswick, 2002, 2020). It is important to mention that sulfide-sulfide liquid immiscibility does not preclude fractionation in the sulfide system, but complements it. Two unmixed trends for Cu-poor and Cu-rich mineralizations on Ni/S vs. Cu/S (at%) diagram were shown by Beswick, (2002, 2020) for McCreedy West ores, Sudbury. According to his results, the data of the Cu-poor and Cu-rich McCreedy West ores are overlaid with different compositions of the immiscible sulfide melts produced experimentally by Ballhaus et al. (2001).

Although sulfide-sulfide liquid immiscibility has still not been proven, and fractional crystallization is a more plausible mechanism to describe a global zonation of Cu-poor and Cu-rich ores in Cu-Ni-PGE deposits, Mt. Rudnaya globular ISS-MSS ores argue in favor of the possibility of the immiscibility between different sulfide liquids. In our proposed hypothesis, ISS and MSS globules were not formed by the gradual crystallization of different generations of sulfide liquids. An unmixing of ISS globules, MSS globules, and MSS-ISS matrix apparently was due to partial immiscibility of initially separated liquids, which were crystallized and equilibrated after separation. Peritectic origin of contact Pd-rich pentlandite from inner rims of ISS globules, suggested by Brovchenko et al. (2020) appears to be in agreement with our proposal. Mt. Rudnaya high form pentlandite could be formed by peritectic reaction between MSS outward bands and Cu-rich liquid globule. Additional evidence for the possible formation of ISS globules from not-equilibrated liquid has also been demonstrated in LA-ICP-MS maps [shown in

Brovchenko et al. (2020)]. Their results show that Co, Zn, and In have direct zonal distribution in the ISS globules, suggesting that the ISS globules crystallize out of a separated liquid phase. A strong heterogeneity of Mt. Rudnaya MSS-ISS ores may have been caused by initial immiscibility and formation of sulfide liquids of different compositions. However, the difference between these first separated liquids is rather negligible (Ballhaus et al., 2001). This process could control the behavior of trace elements at the first steps of the sulfide liquid evolution. More likely, the sulfide-sulfide liquid immiscibility occurs under certain conditions, which in most cases are unattainable during experimental studies or cannot be observed due to the difficulty of quenching the sulfide liquid at high temperatures. Mt. Rudnaya ore-forming liquid was characterized by the exceptional concentrations of Ni, Cu and PGEs. MSS from MSS-ISS ores contains 19–35 wt% of Ni and proportions of ISS dominates over MSS (Distler et al., 1996; Brovchenko et al., 2020). This could be the reason for the absence of ISS globules in many other samples of Mt. Rudnaya MSS-ISS ores and the rare achievement of the immiscibility of two liquids in the experiments of Fe-Ni-Cu-S system.

PGM Distribution

The results obtained by micro-CT show that samples of about 2 × 5 mm may contain up to 815 discrete minerals of platinum and palladium. Most of the PGM were found in ISS globules, whereas the MSS-ISS matrix contains about four times fewer PGM. A difference in PGM occurrence between MSS and ISS imply small-scale variable distributional behavior of PGE in MSS and ISS, respectively. This in turn would suggest the existence of specific conditions for the formation of PGM in Cu-rich ISS globules. Our observations are consistent with the high compatibility of Pt-Pd PGE with Cu-rich liquid (Liu and Brenan, 2015).

Variabilities between the PGM distribution are also observed in the different types of ores. For example in the disseminated ores of Norilsk-Talnakh, the most common PGM are isoferroplatinum (Pt₃Fe) and cooperite (PtS) whereas, in the massive ores Pd minerals are more common (Genkin and Evstigneeva, 1986). Although the mechanism of PGM formation is still not clear, it is believed that isoferroplatinum and cooperite are the earliest PGM forming at high temperatures (Genkin and Evstigneeva, 1986). However, the majority of Norilsk-Talnakh ores were altered through secondary processes by hydrothermal fluids to varying degrees. Platinum and Pd show high mobility in hydrothermal chloride-bearing fluids (Tagirov et al., 2015, 2019), and PGM from the Norilsk-Talnakh ores are sometimes associated with the secondary Cl-bearing sulfide djferfisherite (K₆(Fe,Cu,Ni)₂₅S₂₆Cl) (Genkin and Evstigneeva, 1986). Moreover, primary PGMs also can be redistributed by hydrothermal transfer due to the desulfurization processes (Polovina et al., 2004).

Mt. Rudnaya MSS-ISS ores do not show signs of hydrothermal reworking and rather represent a product of rapid quenching of the magmatic sulfide liquids. PGM associations from Mt. Rudnaya offshoot ores correspond to the typical unaltered Norilsk 1 massive ores and can be divided into two thermodynamic systems (Genkin and Evstigneeva, 1986;

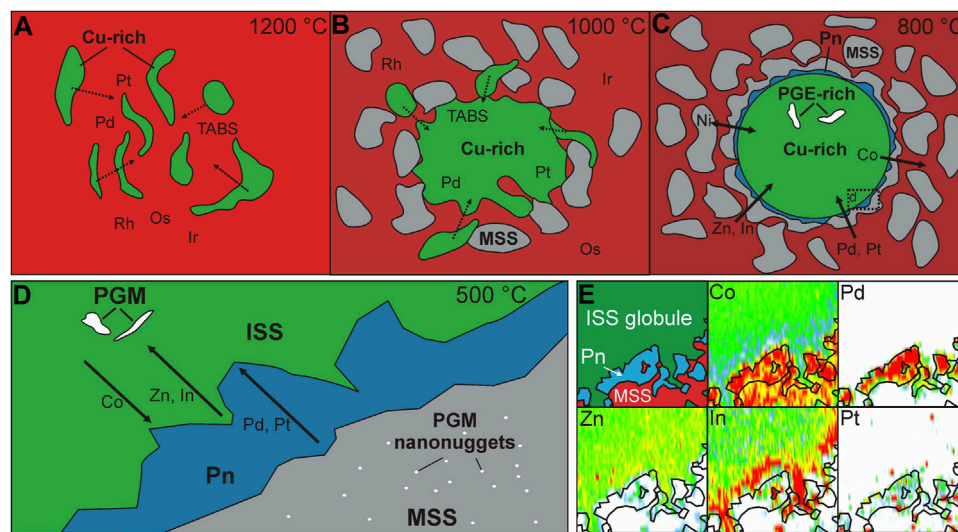


FIGURE 7 | Schematic model of the formation of ISS globules for the investigated samples; **(A)**: Cu-rich liquid (green) gathers together to form a globule with elements as Pt, Pd and TABS; **(B)**: Cu-poor liquid (red) starts to crystallize MSS (grey); **(C)**: Formation of an MSS rim around the ISS globule, with pentlandite (pn) formation at the contact between MSS and Cu-rich liquid; **(D)**: Detailed view of the contact between MSS and ISS, with large PGM grains in the ISS and PGM nanonuggets in the MSS; **(E)**: LA-ICP-MS maps of the MSS-ISS contact with the distribution of different elements (Brovchenko et al., 2020).

Sluzhenikin et al., 2020). Tetraferroplatinum, Pt_3Fe_2 , Pt_2Fe , and cooperite can be considered as members of a Pt-Fe-S system (Majzlan et al., 2002) while atokite and rustenburgite as members of the Pt-Pd-Sn phase system (Shelton et al., 1981). Both systems are stable over a wide temperature range. Experimental studies in the Pt-Pd-Sn system specified the upper temperature of formation for atokite at 1,326°C and rustenburgite at 1,406°C (Shelton et al., 1981). Also for zoned Norilsk-Talnakh PGM intergrowths of the Pt-Pd-Cu stannides in Cu-rich massive ores it was established that atokite and rustenburgite were the earliest PGM and were formed before increasing in the Cu activity (Barkov et al., 2000). Though the association of Pt-Pd-Cu stannides is a very common feature for Norilsk-Talnakh (Razin, 1976), we did not observe Pt-Pd-Cu-Sn minerals in Mt. Rudnaya MSS-ISS ores. The temperatures of Pt-Pd-Cu stannides crystallization are much lower than for atokite and rustenburgite with the maximum at 550°C for stannopalladinite $(Pd,Pt)_5CuSn_2$ (Evstigneeva and Nekrasov, 1984). We assume that an absence of Pt-Pd-Cu stannides in Mt. Rudnaya Cu-rich MSS-ISS ores could be proof of the primary origin of atokite and rustenburgite at the high temperatures.

Tetraferroplatinum is one end-members of the Fe-Pt-S solid solutions, while Pt_3Fe_2 and Pt_2Fe are common in nature (Cabri et al., 1996; Malitch and Thalhammer, 2002; Sluzhenikin et al., 2020), they are not observed in experiments (Cabri and Feather, 1975; Massalski et al., 1986; Majzlan et al., 2002). It is important for this system that platinum phases coexist with MSS. According to experimental studies, an eutectic temperature for $Fe_{1-x}S$ - Pt_3Fe -PtS join is 1,050°C (Bryukvin, 1987) and the solubility of Pt in MSS increases with temperature (Ballhaus and Ulmer, 1995; Majzlan et al., 2002). The solubility of Pt in MSS also depends on the MSS chemical composition as the most nonstoichiometric MSS accommodates more Pt than the stoichiometric MSS (Makovicky

et al., 1986, 1988; Bryukvin, 1987). In contrast to MSS, the solubility of PGE in ISS is very poor (Karup-Møller et al., 2008). Upon quenching Pt in the unknown phase exsolves from MSS forming “dusting” round particles hardly distinguished at EPMA (Majzlan et al., 2002; Peregoedova et al., 2004). Makovicky et al. (1988) reported exsolution of similar small particles of Pd phases in Pd-rich MSS at 900°C. MSS from Mt. Rudnaya ores contains up to 65 ppm of Pt and 168 ppm of Pd heterogeneously distributed in the grains (Brovchenko et al., 2020). According to experimental studies, Pt and Pd are not compatible with MSS (Liu and Brennan, 2015) thereby the existence of nanonuggets of PGM in MSS is very probable (Majzlan et al., 2002; Wirth et al., 2013). Due to the rapid quenching of the Mt. Rudnaya liquids, the PGE should not have been significantly redistributed by diffusion from both MSS and ISS. Outward migration was recorded only for Pd at 300°C (Makovicky et al., 1988) and can be possibly reflected in the contact with pentlandite grains. The Pd content varies significantly within pentlandite grains from Mt. Rudnaya ores, increasing from the contact with MSS towards the contact with ISS (Brovchenko et al., 2020).

Following the evidence discussed, it is obvious that the PGM associations of the MSS-ISS ores of Mt. Rudnaya are of primary magmatic origin and not hydrothermal. Neither texture changes nor exsolutions in solid solutions are detectable, which indicates hydrothermal transformations. Instead, it is more probable that most of the PGM were trapped at the stage of Cu-rich liquid globules formation or were formed *in-situ* in ISS-globules from PGE-rich liquid. Our second suggestion involves that ISS globules could not dissolve PGE in contrast to MSS and pentlandite which are expected to be characterized by high contents of PGE according to Brovchenko et al. (2020). The issue of the PGE solubility in natural sulfides is still debated (Filimonova et al., 2019). Another way of PGE incorporation into sulfides is the formation of PGM nanonuggets

(Kosyakov et al., 2012; Wirth et al., 2013; Junge et al., 2015). Despite the exceptional resolution of the micro-CT scans, it is very challenging to recognize nanonuggets of PGM in sulfides. For a detailed analysis of these nanonuggets, smaller sample sizes are required to achieve sub-micrometer resolution. Nevertheless, a comparison in size of PGM in ISS globules and ISS-MSS matrix displays that the smallest grains mostly occur in the ISS-MSS matrix (**Figure 5C**).

In any case, the behavior of PGE is expected to be controlled by partition coefficients. This means that the PGE could have been distributed mostly into Cu-rich liquid (which formed ISS later) at the very beginning (Ballhaus et al., 2001). This might be the reason why the ISS globules are enriched in PGM, but ISS from ISS-MSS matrix is not. An alternative addition to this hypothesis is that ISS globules could have been formed by immiscibility in the fractionated sulfide liquid and trapped the major part of the PGM inclusions or PGE-rich liquid. Thus, heterogeneity in PGM distribution between Fe-Ni-rich and Cu-rich ores, which is well known for Norilsk-Talnakh deposits, is observed even in the small-scaled textured ISS-MSS ores and was likely caused by both, the difference in PGE partitioning between Cu-rich and Cu-poor phases, and the ability of Fe-Ni-rich phases to dissolve PGE.

ISS Globules Formation

Our proposed model of the formation of ISS globules is presented in **Figure 7**. At superliquidus temperatures, the initial sulfide liquid separates into two immiscible liquids (**Figure 7A**). The green-labelled Cu-rich liquid gathers together with compatible elements such as Pt, Pd, and TABS to form a globule, whereas the Cu-poor liquid starts to crystallize MSS at 950°C (**Figure 7B**). These two immiscible liquids have similar compositions, with the Cu-rich liquid containing Ni and Fe, and the Cu-poor liquid containing Cu and Ni (Ballhaus et al., 2001). But despite this, they are immiscible starting at the superliquidus temperatures. The area around the globule becomes depleted in Cu-rich components and this depleted liquid can only form MSS, leading to the formation of an MSS rim around the ISS globule (**Figure 7C**). Nickel is incompatible with Fe-rich liquid and is concentrated at the contact between MSS and the Cu-rich liquid. This eventually leads to pentlandite formation by a peritectic reaction at 865°C (Kitakaze et al., 2016) or later by exsolution from the MSS at 450°C (Helmy et al., 2021). Crystallization of MSS enriches the originally Cu-poor liquid with Cu by fractional crystallization. The remaining sulfide liquid acquires enough Cu to crystallize ISS at 700°C from the ISS-MSS matrix. The major part of Pt and Pd is partitioned into the Cu-rich liquid at superliquidus temperatures. Platinum, Pd, and TABS occur in an independent liquid, which is immiscible with the Cu-rich liquid in the globule (**Figure 7C**). Upon cooling the PGE-rich liquid forms PGM up to 120 μm in size (**Figure 7D**). The minor part of Pt and Pd and also Rh, Ir, and Os remains in Cu-poor liquid at the very beginning and is dissolved in MSS and residual liquid for a long temperature range unless forming PGM nanonuggets at quenching (**Figure 7D**). As a result of these complicated multiple processes, the ores become highly heterogeneous. Major and trace elements diffuse into coherent phases making directional trends of enrichment (**Figures 7D,E**), which was demonstrated by Brovchenko et al. (2020) at LA-ICP-MS distributional maps (**Figure 7E**).

SUMMARY AND CONCLUSION

We have shown that X-ray micro-CT is a powerful tool for the investigation of trace phases such as Platinum group minerals. Furthermore, the combination of micro-CT and sp-CT allows the identification and distribution of specific elements in 3D, which enables the identification of different minerals. A combination of X-ray micro-CT and sp-CT could be used as a first analysis step of large samples and specific regions could then be used for further investigation using high-resolution 2D methods such as SEM. As an additional method in the routine characterization of ores, micro-CT helps to understand the 3D distribution of different minerals and could be used to extract 3D properties of ore minerals for the simulation of potential processing steps. Nevertheless, there are some limitations in terms of detecting small minerals due to the spatial resolving power and detecting elements with $Z < 47$ due to the measurable energy range using the spectral detector. Therefore, this combination of techniques is of particular interest for the characterization of ores with highly attenuating ore minerals.

Moreover, we proposed a new model for the formation of ISS globules for the Mt. Rudnaya ores. But additional X-ray CT studies with sub-micron resolution are necessary to investigate the distribution of PGM nanonuggets in the samples, which could help for a better understanding of PGE incorporation into sulfides.

DATA AVAILABILITY STATEMENT

The raw data supporting the conclusions of this article will be made available by the authors, without undue reservation.

AUTHOR CONTRIBUTIONS

JS performed the SEM-EDS scans and the data analysis of the SEM-EDS and the computed tomography scans. Moreover, he did the layout for the manuscript and wrote the introduction, materials and methods, results, and parts of the discussion. VB wrote the geological background and the discussion. AS helped with the data analysis of the computed tomography scan and wrote a part of the materials and methods section. FB performed the SEM-EDS scans and helped with the data analysis. MB performed the computed tomography scans and helped with the data analysis. AR helped with the corrections and the wording of the manuscript. VC also helped with the corrections and the wording of the manuscript. MM helped with the computed tomography scans and the data analysis and the corrections of the manuscript. SS helped with the corrections and the wording of the manuscript.

FUNDING

This research is part of the upscaling project “Resource Characterization: from 2D to 3D microscopy” and has received funding from the European Institute of Innovation and Technology (EIT), a body of the European Union, under the Horizon 2020, the EU Framework Program for Research and Innovation. The study at IGEM RAS was supported by the Russian Science Foundation (grant 21-17-00119). The number of the 2D3Dscopy project is 1802.

REFERENCES

- Arndt, N. T. (2011). Insights into the Geologic Setting and Origin of Ni-Cu-PGE Sulfide Deposits of the Norilsk-Talnakh Region, Siberia. *Magmat. Ni-cu PGE Depos. Geol. Geochemistry, Genes.* 17 (0). doi:10.5382/Rev.17
- Augé, T. (1988). Platinum-group Minerals in the Tiebaghi and Vourinos Ophiolitic Complexes; Genetic Implications. *Can. Mineral.* 26, 177–192.
- Badran, A., Marshall, D., Legault, Z., Makovetsky, R., Provencher, B., Piché, N., et al. (2020). Automated Segmentation of Computed Tomography Images of Fiber-Reinforced Composites by Deep Learning. *J. Mater. Sci.* 55, 16273–16289. doi:10.1007/s10853-020-05148-7
- Ballhaus, C., Tredoux, M., and Späth, A. (2001). Phase Relations in the Fe-Ni-Cu-PGE-S System at Magmatic Temperature and Application to Massive Sulphide Ores of the Sudbury Igneous Complex*. *J. Petrol.* 42, 1911–1926. doi:10.1093/ptetrology/42.10.1911
- Ballhaus, C., and Ulmer, P. (1995). Platinum-group Elements in the Merensky Reef: II. Experimental Solubilities of Platinum and Palladium in Fe1-xS from 950 to 450°C under Controlled and. *Geochimica et Cosmochimica Acta* 59, 4881–4888. doi:10.1016/0016-7037(95)00355-X
- Barkov, A. Y., Martin, R. F., Poirier, G., and Yakovlev, Y. N. (2000). The Taimyrite-Tatyanite Series and Zoning in Intermetallic Compounds of Pt, Pd, Cu, and Sn from Noril'sk, Siberia, Russia. *Can. Mineral.* 38, 599–609. doi:10.2113/gscanmin.38.3.599
- Barnes, S.-J., Cox, R. A., and Zientek, M. L. (2006). Platinum-group Element, Gold, Silver and Base Metal Distribution in Compositionally Zoned Sulfide Droplets from the Medvezky Creek Mine, Noril'sk, Russia. *Contrib. Mineral. Petrol.* 152, 187–200. doi:10.1007/s00410-006-0100-9
- Barnes, S.-J., and Lightfoot, P. C. (2005). Formation of Magmatic Nickel Sulfide Deposits and Processes Affecting Their Copper and Platinum Group Element Contents. *Econ. Geol.* 100, 179–213. doi:10.5382/AV100.08
- Barnes, S. J., Le Vaillant, M., Godel, B., and Leshner, C. M. (2019). Droplets and Bubbles: Solidification of Sulphide-Rich Vapour-Saturated Orthocumulates in the Norilsk-Talnakh Ni-Cu-PGE Ore-Bearing Intrusions. *J. Petrol.* 60, 269–300. doi:10.1093/ptetrology/egy114
- Barnes, S. J., Malitch, K. N., and Yudovskaya, M. A. (2020a). Introduction to a Special Issue on the Norilsk-Talnakh Ni-Cu-Platinum Group Element Deposits. *Econ. Geol.* 115, 1157–1172. doi:10.5382/ECONGEO.4750
- Barnes, S. J., Mungall, J. E., Le Vaillant, M., Godel, B., Leshner, C. M., Holwell, D., et al. (2017). Sulfide-silicate Textures in Magmatic Ni-Cu-PGE Sulfide Ore Deposits: Disseminated and Net-Textured Ores. *Am. Mineral.* 102, 473–506. doi:10.2138/am-2017-5754
- Barnes, S. J., Taranovic, V., Schoneveld, L. E., Mansur, E. T., Le Vaillant, M., Dare, S., et al. (2020b). The Occurrence and Origin of Pentlandite-Chalcopyrite-Pyrrhotite Loop Textures in Magmatic Ni-Cu Sulfide Ores. *Econ. Geol.* 115, 1777–1798. doi:10.5382/econgeo.4757
- Beswick, A. E. (2002). An Analysis of Compositional Variations and Spatial Relationships within Fe-Ni-Cu Sulfide Deposits on the North Range of the Sudbury Igneous Complex. *Econ. Geol.* 97, 1487–1508. doi:10.2113/gsecongeo.97.7.1487
- Beswick, A. E. (2020). Component Element Ratio Analysis of the McCreey West Fe-Ni-Cu Sulfide deposit, North Range of the Sudbury Igneous Complex. *SN Appl. Sci.* 2, 1–9. doi:10.1007/s42452-020-2798-9
- Boone, M. N., Garrovoet, J., Tack, P., Scharf, O., Cormode, D. P., Van Loo, D., et al. (2014). High Spectral and Spatial Resolution X-ray Transmission Radiography and Tomography Using a Color X-ray Camera. *Nucl. Instr. Methods Phys. Res. Section A: Acc. Spectrometers, Detectors Associated Equipment* 735, 644–648. doi:10.1016/j.nima.2013.10.044
- Breiman, L. (2001). Random Forests. *Mach. Learn.* 45, 5–32. doi:10.1023/A:1010933404324
- Brenan, J. M., Haider, N., and Andrews, D. (2008). Experimental Evaluation of Liquid Immiscibility in a Portion of the System Fe-Ni-Cu-S Using High Gravitational Acceleration. *Econ. Geology.* 103, 1563–1570. doi:10.2113/gsecongeo.103.7.1563
- Brovchenko, V. D., Sluzhenikin, S. F., Kovalchuk, E. V., Kovrigina, S. V., Abramova, V. D., and Yudovskaya, M. A. (2020). Platinum Group Element Enrichment of Natural Quenched Sulfide Solid Solutions, the Norilsk 1 Deposit, Russia. *Econ. Geol.* 115, 1343–1361. doi:10.5382/ECONGEO.4741
- Bryukvin, V. (1987). Investigation of Phase Diagram of Fe-Pt-S System. *Izv. Akad. Nauk SSSR* 4, 25–30.
- Bultreys, T., De Boever, W., and Cnudde, V. (2016). Imaging and image-based fluid transport modeling at the pore scale in geological materials: A practical introduction to the current state-of-the-art. *Earth-Science Rev.* 155, 93–128. doi:10.1016/j.earscirev.2016.02.001
- Burgess, S. D., and Bowring, S. A. (2015). High-precision geochronology confirms voluminous magmatism before, during, and after Earth's most severe extinction. *Sci. Adv.* 1. doi:10.1126/sciadv.1500470
- Cabri, L. J., and Feather, C. E. (1975). Platinum-iron alloys; a nomenclature based on a study of natural and synthetic alloys. *Can. Mineral.* 13, 117–126.
- Cabri, L. J., Harris, D. C., and Weiser, T. W. (1996). Mineralogy and distribution of platinum-group mineral (PGM) placer deposits of the world. *Explor. Min. Geol.* 5, 73–167.
- Cabri, L. J. (1973). New data on Phase Relations in the Cu-Fe-S System. *Econ. Geol.* 68, 443–454. doi:10.2113/gsecongeo.68.4.443
- Cafagna, F. (2015). *The Geochemical Behavior of Metalloids and Their Effect on the Highly Siderophile Elements during the Crystallization of a Magmatic Sulfide Liquid in Relation to the Formation of Ni-Cu-PGE Magmatic Sulfide Deposits.*
- Chantler, C. T. (2001). Detailed tabulation of atomic form factors, photoelectric absorption and scattering cross section, and mass attenuation coefficients in the vicinity of absorption edges in the soft X-ray (Z= 30-36, Z= 60-89, E= 0.1-10 keV) - addressing convergence issues of earlier work. *J. Synchrotron Radiat.* 8, 1124. doi:10.1107/S0909049501008305
- Chen, S., Wu, X., Wang, Q., and Fang, Z. (2017). "Study on the material recognition of the region of interest by hyperspectral CT reconstruction methods," in The 9th International Symposium on NDT in Aerospace, 1–8.
- Chetty, D., Clark, W., Bushell, C., Sebola, T. P., Hoffman, J., Nshimirimana, R., et al. (2012). The Use of 3D X-Ray Computed Tomography for Gold Location in Exploration Drill Cores. *Proc. 10th Int. Congr. Appl. Mineral.*, 129–136. doi:10.1007/978-3-642-27682-8_17
- Cnudde, V., and Boone, M. N. (2013). High-resolution X-ray computed tomography in geosciences: A review of the current technology and applications. *Earth-Science Rev.* 123, 1–17. doi:10.1016/j.earscirev.2013.04.003
- Cnudde, V., Masschaele, B., Dierick, M., Vlassenbroeck, J., Hoorebeke, L. V., and Jacobs, P. (2006). Recent progress in X-ray CT as a geosciences tool. *Appl. Geochem.* 21, 826–832. doi:10.1016/j.apgeochem.2006.02.010
- Craig, J. R., and Kullerud, G. (1969). Phase Relations in the Cu-Fe-Ni-S System and Their Application to Magmatic Ore Deposits. *Magmat. Ore Depos.* 4, 0. doi:10.5382/Mono.04.25
- Czamanske, G. K., Kunilov, V. E., Zientek, M. L., Cabri, L. J., Likhachev, A. P., Calk, L. C., et al. (1992). A proton microprobe study of magmatic sulfide ores from the Noril'sk-Talnakh District, Siberia. *Can. Mineral.* 30, 249–287.
- Dare, S. A. S., Barnes, S.-J., and Prichard, H. M. (2010). The distribution of platinum group elements (PGE) and other chalcophile elements among sulfides from the Creighton Ni-Cu-PGE sulfide deposit, Sudbury, Canada, and the origin of palladium in pentlandite. *Miner Deposita* 45, 765–793. doi:10.1007/s00126-010-0295-6
- De Boever, W., Derluyn, H., Van Loo, D., Van Hoorebeke, L., and Cnudde, V. (2015). Data-fusion of high resolution X-ray CT, SEM and EDS for 3D and pseudo-3D chemical and structural characterization of sandstone. *Micron* 74, 15–21. doi:10.1016/j.micron.2015.04.003
- Devadithya, S., and Castañón, D. (2021). Enhanced Material Estimation with Multi-Spectral CT. *ei* 33, 229–12297. doi:10.2352/issn.2470-1173.2021.15.coimg-229
- Distler, V. V., Genkin, A. D., and Dyuzhikov, O. A. (1986). "Sulfide Petrology and Genesis of Copper-Nickel Ore Deposits," in *Geology and Metallogeny of Copper Deposits.* Editors G. H. Friedrich, A. D. Genkin, A. J. Naldrett, J. D. Ridge, R. H. Sillitoe, and F. M. Vokes (Berlin, Heidelberg: Springer), 111–123. doi:10.1007/978-3-642-70902-9_7
- Distler, V. V., Grokhovskaya, T. L., Evstigneeva, T. L., Sluzhenikin, S. F., Filimonova, A. A., and Dyuzhikov, O. A. (1988). *Petrology of Magmatic Sulfide Ore Formation.* Moscow, Russia: Nauka.
- Distler, V. V., Kulagov, E. A., Sluzhenikin, S. F., and Laputina, I. P. (1996). Quenched Sulfide Solid Solutions in Ores of the Noril'sk Deposit. *Geol. Ore Depos.* 38, 35–46.

- Distler, V. V., Malevsky, A. Y., and Laputina, I. (1977). Distribution of platinoids between pyrrhotite and pentlandite during crystallization of sulfide melt. *Geochem. Int.* 14, 30–40.
- Dodin, D. A., and Batuev, B. N. (1971). “Geology and petrology of the Talnakh differentiated intrusions and their metamorphic aureoles,” in *Petrology and Ore Potential of the Talnakh and Noril'sk Differentiated Intrusions*. Editor N. N. Urvantsev (Leningrad: Nedra), 31–100.
- Dodin, D. A., Batuev, B. N., and Mitenkov, G. A. (1971). *Atlas of the Rocks and Ores of the Noril'sk Copper-Nickel Deposits*. Leningrad: Nedra.
- Duran, C. J., Barnes, S.-J., Pleše, P., Kudrna Prašek, M., Zientek, M. L., and Pagé, P. (2017). Fractional crystallization-induced variations in sulfides from the Noril'sk-Talnakh mining district (polar Siberia, Russia). *Ore Geology. Rev.* 90, 326–351. doi:10.1016/j.oregeorev.2017.05.016
- Duzhikov, O. A., Distler, V. V., Strunin, B. M., Mkrtychyan, A. K., Sherman, M. L., Sluzhenikin, S. S., et al. (1988). Geology and Metallogeny of Sulfide Deposits Noril'sk Region U.S.S.R. U.S.S.R. 1. doi:10.5382/SP.01
- Dyuzhikov, O. A., Distler, V. V., Strunin, B. M., Mkrtychyan, A. K., Sherman, M. L., Sluzhenikin, S. F., et al. (1988). *Geology and Ore Potential of the Norilsk District*. Moscow: Nedra.
- Dyuzhikov, O. A. (2004). The Norilsk PGE-Cu-Ni giant: geological setting, deep structure and petrologic-geodynamic formation model. *Izv. Sektii Nauk o Zemle RAEN* 12, 91–103.
- Ebel, D. S., and Naldrett, A. J. (1996). Fractional crystallization of sulfide ore liquids at high temperature. *Econ. Geol.* 91, 607–621. doi:10.2113/gsecongeo.91.3.607
- Economou-Eliopoulos, M., Eliopoulos, D. G., and Tsoupas, G. (2017). On the diversity of the PGE content in chromitites hosted in ophiolites and in porphyry-Cu systems: Controlling factors. *Ore Geology. Rev.* 88, 156–173. doi:10.1016/j.oregeorev.2017.04.030
- Egan, C. K., Jacques, S. D. M., Wilson, M. D., Veale, M. C., Seller, P., Beale, A. M., et al. (2015). 3D chemical imaging in the laboratory by hyperspectral X-ray computed tomography. *Sci. Rep.* 5. doi:10.1038/srep15979
- Evstigneeva, T. L., and Genkin, A. D. (1983). Cabriite Pd₂SnCu, a new species in the mineral group of palladium, tin and copper compounds. *Can. Mineral.* 21, 481–487.
- Evstigneeva, T. L., and Nekrasov, N. Y. (1984). “Conditions of the formation of tin-bearing platinum-group minerals in the system Pd-Cu-Sn and its partial cross sections,” in *Tin in Magmatic and Postmagmatic Processes*. Editor N. Y. Nekrasov (Moscow: Nauka Press), 143–170.
- Fang, Z., Zhong, S., Wang, R., Ding, L., and Chen, S. (2019). Non-reference evaluation of hyperspectral X-CT images based on CdTe photon counting detector. *ACM Int. Conf. Proceeding Ser.*, 59–63. doi:10.1145/3364836.3364849
- Farrow, C. E. G., and Watkinson, D. H. (1997). Diversity of precious-metal mineralization in footwall Cu-Ni-PGE deposits, Sudbury, Ontario; implications for hydrothermal models of formation. *Can. Mineral.* 35, 817–839.
- Filimonova, O. N., Nickolsky, M. S., Trigub, A. L., Chareev, D. A., Kvashnina, K. O., Kovalchuk, E. V., et al. (2019). The state of platinum in pyrite studied by X-ray absorption spectroscopy of synthetic crystals. *Econ. Geol.* 114, 1649–1663. doi:10.5382/econgeo.4686
- Fiorentini, M. L., Stone, W. E., Beresford, S. W., and Barley, M. E. (2004). Platinum-group element alloy inclusions in chromites from Archaean mafic-ultramafic units: Evidence from the Abitibi and the Agnew-Wiluna Greenstone Belts. *Mineralogy Petrology* 82, 341–355. doi:10.1007/s00710-004-0044-6
- Fleet, M. E., Chrissyoulis, S. L., Stone, W. E., and Weisener, C. G. (1993). Partitioning of platinum-group elements and Au in the Fe?Ni?Cu?S system: experiments on the fractional crystallization of sulfide melt. *Contr. Mineral. Petrol.* 115, 36–44. doi:10.1007/BF00712976
- Fleet, M. E. (1977). Origin of disseminated copper-nickel sulfide ore at Frood, Sudbury, Ontario. *Econ. Geol.* 72, 1449–1456. doi:10.2113/gsecongeo.72.8.1449
- Fleet, M. E., and Stone, W. E. (1991). Partitioning of platinum-group elements in the Fe-Ni-S system and their fractionation in nature. *Geochimica et Cosmochimica Acta* 55, 245–253. doi:10.1016/0016-7037(91)90415-2
- Genkin, A. D., Distler, V. V., Gladyshev, G. D., Filimonova, A. A., Evstigneeva, T. L., Kovalenker, V. A., et al. (1981). *Sulfide Copper-Nickel Ores of the Noril'sk Deposits*. Moscow, Russia: Nauka.
- Genkin, A. D., and Evstigneeva, T. L. (1986). Associations of platinum-group minerals of the Noril'sk copper-nickel sulfide ores. *Econ. Geol.* 81, 1203–1212. doi:10.2113/gsecongeo.81.5.1203
- Godel, B., and Barnes, S.-J. (2008). Platinum-group elements in sulfide minerals and the whole rocks of the J-M Reef (Stillwater Complex): Implication for the formation of the reef. *Chem. Geology.* 248, 272–294. doi:10.1016/j.chemgeo.2007.05.006
- Godel, B., Barnes, S. J., Barnes, S.-J., and Maier, W. D. (2010). Platinum ore in three dimensions: Insights from high-resolution X-ray computed tomography. *Geology* 38, 1127–1130. doi:10.1130/G31265.1
- Godel, B. (2013). High-resolution X-ray computed tomography and its application to ore deposits: From data acquisition to quantitative three-dimensional measurements with case studies from Ni-Cu-PGE Deposits. *Econ. Geology.* 108, 2005–2019. doi:10.2113/econgeo.108.8.2005
- Godinho, J. R. A., Kern, M., Renno, A. D., and Gutzmer, J. (2019). Volume quantification in interphase voxels of ore minerals using 3D imaging. *Minerals Eng.* 144, 106016. doi:10.1016/j.mineng.2019.106016
- Godinho, J. R. A., Westaway-Heaven, G., Boone, M. A., and Renno, A. D. (2021). Spectral Tomography for 3D Element Detection and Mineral Analysis. *Minerals* 11. doi:10.1007/978-1-4020-3995-9_35910.3390/min11060598
- Godlevsky, M. N. (1959). *Traps and Ore-Bearing Intrusions of the Noril'sk Region*, 68. Moscow: Gosgeoltekhizdat.
- Gorbachev, N., and Nekrasov, A. N. (2004). Layering of Fe-Ni-Cu sulfide melts: Experimental study and geological implications. *Dokl. Earth Sci.* 399, 1256–1259.
- Helmy, H. M., Ballhaus, C., Berndt, J., Bockrath, C., and Wohlgemuth-Ueberwasser, C. (2007). Formation of Pt, Pd and Ni tellurides: Experiments in sulfide-telluride systems. *Contrib. Mineral. Petrol.* 153, 577–591. doi:10.1007/s00410-006-0163-7
- Helmy, H. M., Botcharnikov, R., Ballhaus, C., Deutsch-Zemlitskaya, A., Wirth, R., Schreiber, A., et al. (2021). Evolution of magmatic sulfide liquids: how and when base metal sulfides crystallize? *Contrib. Mineral. Petrol.* 176, 1–15. doi:10.1007/s00410-021-01868-4
- Higgins, M. D. (2000). Measurement of crystal size distributions. *Am. Mineral.* 85, 1105–1116. doi:10.2138/am-2000-8-901
- Hill, R., Blenkinsopp, P., Thompson, S., Vickerman, J., and Fletcher, J. S. (2011). A new time-of-flight SIMS instrument for 3D imaging and analysis. *Surf. Interf. Anal.* 43, 506–509. doi:10.1002/sia.3562
- Holwell, D. A., and McDonald, I. (2010). A review of the behaviour of platinum group elements within natural magmatic sulfide ore systems. *Platinum Met. Rev.* 54, 26–36. doi:10.1595/147106709X480913
- Hrstka, T., Gottlieb, P., Skála, R., Breiter, K., and Motl, D. (2018). Automated mineralogy and petrology - applications of TESCAN Integrated Mineral Analyzer (TIMA). *J. Geosci.* 63, 47–63. doi:10.3190/jgeosci.250
- Junge, M., Wirth, R., Oberthür, T., Melcher, F., and Schreiber, A. (2015). Mineralogical siting of platinum-group elements in pentlandite from the Bushveld Complex, South Africa. *Miner Deposita* 50, 41–54. doi:10.1007/s00126-014-0561-0
- Karup-Møller, S., Makovicky, E., and Barnes, S.-J. (2008). The metal-rich portions of the phase system Cu-Fe-Pd-S at 1000°C, 900°C and 725°C: implications for mineralization in the Skaergaard intrusion. *Mineral. Mag.* 72, 941–951. doi:10.1180/minmag.2008.072.4.941
- Keller, L. M., Holzer, L., Wepf, R., Gasser, P., Münch, B., and Marschall, P. (2011). On the application of focused ion beam nanotomography in characterizing the 3D pore space geometry of Opalinus clay. *Phys. Chem. Earth, Parts A/B/C* 36, 1539–1544. doi:10.1016/j.pce.2011.07.010
- Kelly, T. F., and Miller, M. K. (2007). Atom probe tomography. *Rev. Scientific Instr.* 78, 031101. doi:10.1063/1.2709758
- Ketcham, R. A., and Carlson, W. D. (2001). *Acquisition, Optimization and Interpretation of X-ray Computed Tomographic Imagery: Applications to the Geosciences*.
- Kheirabadi, M., Bjorholm Dahl, A., Lund Olsen, U., Mustafa, W., and Lyksborg, M. (2017). “Multispectral x-ray CT: multivariate statistical analysis for efficient reconstruction,” in Proc. SPIE 10391, Developments in X-Ray Tomography XI, 1039113, San Diego, CA, October 6, 2017. Editors B. Müller. and G. Wang (SPIE), 146–156. doi:10.1117/12.2273338
- Kinloch, E. D. (1982). Regional trends in the platinum-group mineralogy of the critical zone of the Bushveld Complex, South Africa. *Econ. Geol.* 77, 1328–1347. doi:10.2113/gsecongeo.77.6.1328
- Kitakaze, A., Machida, T., and Komatsu, R. (2016). Phase Relations In the Fe-Ni-s System From 875 To 650 °C. *Can. Mineral.* 54, 1175–1186. doi:10.3749/canmin.1500087

- Knoll, G. F. (2000). *Radiation Detection and Measurement*. New York: John Wiley & Sons.
- Kosyakov, F. I., Sinyakova, E. F., and Distler, V. V. (2012). Experimental simulation of phase relationships and zoning of magmatic nickel-copper sulfide Ores, Russia. *Geol. Ore Deposits* 54, 179–208. doi:10.1134/S1075701512030051
- Kosyakov, V. I., Sinyakova, E. F., and Nenashev, B. G. (2001). A mechanism of pentlandite formation in the Fe-Ni-S system. *Dokl. Earth Sci.* 381, 1113–1115.
- Kotlitsky, V. K. (1946). Problem of the origin of magmatic copper-nickel deposits. *Dokl. Ross. Akad. Nauk* 51, 814–817.
- Krivolutskaya, N., Tolstykh, N., Kedrovskaya, T., Naumov, K., Kubrakova, I., Tyutyunnik, O., et al. (2018). World-class PGE-Cu-Ni Talnakh deposit: New data on the structure and unique mineralization of the south-western branch. *Minerals* 8, 124. doi:10.3390/min8040124
- Kubis, A. J., Shiflet, G. J., Hull, R., and Dunn, D. N. (2004). Focused ion-beam tomography. *Metall. Mat. Trans. A* 35, 1935–1943. doi:10.1007/s11661-004-0142-4
- Latyshev, A. V., Rad'ko, V. A., Veselovskiy, R. V., Fetisova, A. M., and Pavlov, V. E. (2020). Correlation of the Permian-Triassic Ore-Bearing Intrusions of the Norilsk Region with the Volcanic Sequence of the Siberian Traps Based on the Paleomagnetic Data. *Econ. Geol.* 115, 1173–1193. doi:10.5382/econgeo.4746
- Le Vaillant, M., Barnes, S. J., Mungall, J. E., and Mungall, E. L. (2017). Role of degassing of the Noril'sk nickel deposits in the Permian-Triassic mass extinction event. *Proc. Natl. Acad. Sci. U.S.A.* 114, 2485–2490. doi:10.1073/pnas.1611086114
- Li, C., Naldrett, A. J., Coats, C. J. A., and Johannessen, P. (1992). Platinum, palladium, gold, copper-rich stringers at the Strathcona Mine, Sudbury; their enrichment by fractionation of a sulfide liquid. *Econ. Geol.* 87, 1584–1598. doi:10.2113/gsecongeo.87.6.1584
- Li, C., and Ripley, E. M. (2006). Formation of Pt-Fe alloy by desulfurization of Pt-Pd sulfide in the J-M reef of the Stillwater Complex, Montana. *Can. Mineral.* 44, 895–903. doi:10.2113/gscanmin.44.4.895
- Likhachev, A. (2006). *Platinum-Copper-Nickel and Platinum Deposits*. Moscow, Russia: Eslan.
- Liu, X., Chen, H., Bornefalk, H., Danielsson, M., Karlsson, S., Persson, M., et al. (2015). Energy calibration of a silicon-strip detector for photon-counting spectral CT by direct usage of the X-ray tube spectrum. *IEEE Trans. Nucl. Sci.* 62, 68–75. doi:10.1109/TNS.2014.2373641
- Liu, Y., and Brenan, J. (2015). Partitioning of platinum-group elements (PGE) and chalcogens (Se, Te, As, Sb, Bi) between monosulfide-solid solution (MSS), intermediate solid solution (ISS) and sulfide liquid at controlled fO₂-fS₂ conditions. *Geochimica et Cosmochimica Acta* 159, 139–161. doi:10.1016/j.gca.2015.03.021
- Locmelis, M., Barnes, S. J., Pearson, N. J., and Fiorentini, M. L. (2009). Anomalous sulfur-poor platinum group element mineralization in komatiitic cumulates, Mount Clifford, Western Australia. *Econ. Geology* 104, 841–855. doi:10.2113/gsecongeo.104.6.841
- Majzlan, J., Makovicky, M., Makovicky, E., and Rose-Hansen, J. (2002). The System Fe-Pt-S-AT 1100 C. *Can. Mineral.* 40, 509–517. doi:10.2113/gscanmin.40.2.509
- Makovitsky, R., Piche, N., and Marsh, M. (2018). Dragonfly as a Platform for Easy Image-based Deep Learning Applications. *Microsc. Microanal.* 24, 532–533. doi:10.1017/s143192761800315x
- Makovicky, M., Makovicky, E., and Rose-Hansen, J. (1988). "Experimental Evidence on the Formation and Mineralogy of Platinum and Palladium Ore Deposits BT - Mineral Deposits within the European Community," in eds. J. Boissonnas and P. Omenetto (Berlin, Heidelberg: Springer Berlin Heidelberg), 303–317. doi:10.1007/978-3-642-51858-4_17
- Makovicky, M., Makovicky, E., and Rose-Hansen, J. (1986). "Experimental studies on the solubility and distribution of platinum group elements in base-metal sulphides in platinum deposits," in *Metallogeny of Basic and Ultrabasic Rocks*. Editors M. J. Gallagher, R. A. Ixer, C. R. Neary, and H. M. Prichard (London, U.K.: The Institution of Mining and Metallurgy), 415–425.
- Malitch, K. N., and Thalhammer, O. A. R. (2002). Pt-Fe nuggets Derived From Clinopyroxenite Dunite Massifs, Russia: A Structural, Compositional and Osmium-Isotope Study. *Can. Mineral.* 40, 395–418. doi:10.2113/gscanmin.40.2.395
- Mansur, E. T., Barnes, S.-J., Duran, C. J., and Sluzhenikin, S. F. (2020). Distribution of chalcophile and platinum-group elements among pyrrhotite, pentlandite, chalcopyrite and cubanite from the Noril'sk-Talnakh ores: implications for the formation of platinum-group minerals. *Miner Deposita* 55, 1215–1232. doi:10.1007/s00126-019-00926-z
- Mansur, E. T., Barnes, S.-J., and Duran, C. J. (2019). Textural and compositional evidence for the formation of pentlandite via peritectic reaction: Implications for the distribution of highly siderophile elements. *Geology* 47, 351–354. doi:10.1130/G45779.1
- Mansur, E. T., and Barnes, S.-J. (2020). The role of Te, As, Bi, Sn and Sb during the formation of platinum-group-element reef deposits: Examples from the Bushveld and Stillwater Complexes. *Geochimica et Cosmochimica Acta* 272, 235–258. doi:10.1016/j.gca.2020.01.008
- Massalski, T. B., Okamoto, H., Subramanian, P., Kacprzak, L., and Scott, W. W. (1986). *Binary alloy Phase Diagrams*. Metals Park, Ohio: American Society for Metals.
- McLaren, C. H., and De Villiers, J. P. R. (1982). The platinum-group chemistry and mineralogy of the UG-2 chromitite layer of the Bushveld complex. *Econ. Geol.* 77, 1348–1366. doi:10.2113/gsecongeo.77.6.1348
- Miroshnikova, L. (2017). *Geological and Geochemical Prerequisites and Signs of Localization of Copper-Nickel with Platinoids Mineralization of the Ore-Magmatic System of the Talnakh Ore Sluiter*.
- Mungall, J. E., Andrews, D. R. A., Cabri, L. J., Sylvester, P. J., and Tubrett, M. (2005). Partitioning of Cu, Ni, Au, and platinum-group elements between monosulfide solid solution and sulfide melt under controlled oxygen and sulfur fugacities. *Geochimica et Cosmochimica Acta* 69, 4349–4360. doi:10.1016/j.gca.2004.11.025
- Mungall, J. E., Brenan, J. M., Godel, B., Barnes, S. J., and Gaillard, F. (2015). Transport of metals and sulphur in magmas by flotation of sulphide melt on vapour bubbles. *Nat. Geosci.* 8, 216–219. doi:10.1038/ngeo2373
- Naldrett, A. J., Asif, M., Scandl, E., Searcy, T., Morrison, G. G., Binney, W. P., et al. (1999). Platinum-group elements in the Sudbury ores; significance with respect to the origin of different ore zones and to the exploration for footwall orebodies. *Econ. Geol.* 94, 185–210. doi:10.2113/gsecongeo.94.2.185
- Naldrett, A. J., Lightfoot, P. C., Fedorenko, V., Doherty, W., and Gorbachev, N. S. (1992). Geology and geochemistry of intrusions and flood basalts of the Noril'sk region, USSR, with implications for the origin of the Ni-Cu ores. *Econ. Geol.* 87, 975–1004. doi:10.2113/gsecongeo.87.4.975
- Naldrett, A. J. (2004). *Magmatic Sulfide Deposits: Geology, Geochemistry and Exploration*. Berlin, Heidelberg: Springer, Berlin, Heidelberg. doi:10.1007/978-3-662-08444-1
- Naldrett, A. J. (1999). World-class Ni-Cu-PGE deposits: Key factors in their genesis. *Mineralium Deposita* 34, 227–240. doi:10.1007/s001260050200
- Novikov, A. A., Major, D., Wimmer, M., Lenis, D., and Buhler, K. (2019). Deep sequential segmentation of organs in volumetric medical scans. *IEEE Trans. Med. Imaging* 38, 1207–1215. doi:10.1109/TMI.2018.2881678
- Nygren, H., Hagenhoff, B., Malmberg, P., Nilsson, M., and Richter, K. (2007). Bioimaging TOF-SIMS: High resolution 3D imaging of single cells. *Microsc. Res. Tech.* 70, 969–974. doi:10.1002/jemt.20502
- O'Driscoll, B., and González-Jiménez, J. M. (2016). Petrogenesis of the platinum-group minerals. *Rev. Mineralogy Geochem.* 81, 489–578. doi:10.2138/rmg.2016.81.09
- Peregoedova, A., Barnes, S.-J., and Baker, D. R. (2004). The formation of Pt-Ir alloys and Cu-Pd-rich sulfide melts by partial desulfurization of Fe-Ni-Cu sulfides: results of experiments and implications for natural systems. *Chem. Geology* 208, 247–264. doi:10.1016/j.chemgeo.2004.04.015
- Peregoedova, A. V. (1998). The experimental study of the Pt-Pd-partitioning between monosulfide solid solution and Cu-Ni-sulfide melt at 900–840 °C. in The 8th International Platinum Symposium, 325–373.
- Piche, N., Bouchard, I., and Marsh, M. (2017). Dragonfly SegmentationTrainer - A General and User-Friendly Machine Learning Image Segmentation Solution. *Microsc. Microanal.* 23, 132–133. doi:10.1017/s1431927617001349
- Polovina, J. S., Hudson, D. M., and Jones, R. E. (2004). Petrographic and Geochemical Characteristics of Postmagmatic Hydrothermal Alteration and Mineralization in the J-M Reef, Stillwater Complex, Montana. *Can. Mineral.* 42, 261–277. doi:10.2113/gscanmin.42.2.261
- Potop, A., Rebuffel, V., Rinkel, J., Brambilla, A., Peyrin, F., and Verger, L. (2014). "Investigation of the polynomial approach for material decomposition in spectral X-ray tomography using an energy-resolved detector," in Proc. SPIE 9033, Medical Imaging 2014: Physics of Medical Imaging, 90333I, San Diego, CA, March 19, 2014 (SPIE). doi:10.1117/12.2042133

- Prichard, H. M., Knight, R. D., Fisher, P. C., McDonald, I., Zhou, M.-F., and Wang, C. Y. (2013). Distribution of platinum-group elements in magmatic and altered ores in the Jinchuan intrusion, China: An example of selenium remobilization by postmagmatic fluids. *Miner Deposita* 48, 767–786. doi:10.1007/s00126-013-0454-7
- Raghavan, V. (2004). Cu-Fe-S (Copper-Iron-Sulfur). *J. Phase Equilibria Diffusion* 25, 450–454. doi:10.1361/15477030420845
- Ramsey, M. H. (2021). Challenges for the estimation of uncertainty of measurements made *In Situ*. *Accred Qual. Assur.* 26, 183–192. doi:10.1007/s00769-020-01446-4
- Rao, C. R. M., and Reddi, G. S. (2000). Platinum group metals (PGM); occurrence, use and recent trends in their determination. *Trac Trends Anal. Chem.* 19, 565–586. doi:10.1016/S0165-9936(00)00031-5
- Razin, L. V. (1976). Geologic and genetic features of forsterite dunites and their platinum-group mineralization. *Econ. Geol.* 71, 1371–1376. doi:10.2113/gsecongeo.71.7.1371
- Reyes, F., Lin, Q., Udoudo, O., Dodds, C., Lee, P. D., and Neethling, S. J. (2017). Calibrated X-ray micro-tomography for mineral ore quantification. *Minerals Eng.* 110, 122–130. doi:10.1016/j.mineng.2017.04.015
- Reznikov, N., Buss, D. J., Provencher, B., McKee, M. D., and Piché, N. (2020). Deep learning for 3D imaging and image analysis in biomineralization research. *J. Struct. Biol.* 212, 107598. doi:10.1016/j.jsb.2020.107598
- Roessl, E., Cormode, D., Brendel, B., Jürgen Engel, K., Martens, G., Thran, A., et al. (2011). Preclinical spectral computed tomography of gold nano-particles. *Nucl. Instr. Methods Phys. Res. Section A: Acc. Spectrometers, Detectors Associated Equipment* 648, S259–S264. doi:10.1016/j.nima.2010.11.072
- Ronneberger, O., Fischer, P., and Brox, T. (2015). “U-Net: Convolutional Networks for Biomedical Image Segmentation,” in *Medical Image Computing and Computer-Assisted Intervention – MICCAI 2015*. Editors N. Navab, J. Hornegger, W. M. Wells, and A. F. Frangi (Cham: Springer International Publishing), 234–241. doi:10.1007/978-3-319-24574-4_28
- Roussel, O., Rahmim, A., Alavi, A., and Zaidi, H. (2007). Partial Volume Correction Strategies in PET. *PET. Clin.* 2, 235–249. doi:10.1016/j.cpet.2007.10.005
- Ryabov, V. V., Shevko, A. Y., and Gora, M. P. (2014). *Trap Magmatism and Ore Formation in the Siberian Noril'sk Region*. Springer Dordrecht. doi:10.1007/978-94-007-5022-7
- Shelton, K. L., Merewether, P. A., and Skinner, B. J. (1981). Phases and phase relations in the system Pd-Pt-Sn. *Can. Mineral.* 19, 599–605.
- Sinyakova, E., Kosyakov, V., Distler, V., and Karmanov, N. (2016). Behavior of Pt, Pd, and Au During Crystallization of Cu-rich Magmatic Sulfide Minerals. *Can. Mineral.* 54, 491–509. doi:10.3749/canmin.1500015
- Sittner, J., Godinho, J. R. A., Renno, A. D., Cnudde, V., Boone, M., De Schryver, T., et al. (2020). Spectral X-ray computed micro tomography: 3-dimensional chemical imaging. *X-ray Spectrom.* 50, 92–105. doi:10.1002/xrs.3200
- Sittner, J., Merkulova, M., Godinho, J. R. A., Renno, A. D., Cnudde, V., Boone, M., et al. (2021). “Spectral X-Ray Computed Micro Tomography: 3-Dimensional Chemical Imaging by Using a Pixelated Semiconductor Detector,” in *Radiation Detection Systems*. Editors J. S. Iwaczyk and K. Iniewski (Boca Raton: CRC Press), 28. doi:10.1002/xrs.3200
- Sluzhenikin, S. F., Yudovskaya, M. A., Barnes, S. J., Abramova, V. D., Le Vaillant, M., Petrenko, D. B., et al. (2020). Low-Sulfide Platinum Group Element Ores of the Norilsk-Talnakh Camp. *Econ. Geol.* 115, 1267–1303. doi:10.5382/ECONGEO.4749
- Tagirov, B. R., Baranova, N. N., and Bychkova, Y. V. (2015). Thermodynamic properties of platinum chloride complexes in aqueous solutions: Derivation of consistent parameters from literature data and experiments on Pt(cr) solubility at 400–475°C and 1 kbar. *Geochem. Int.* 53, 327–340. doi:10.1134/S0016702915040084
- Tagirov, B. R., Filimonova, O. N., Trigub, A. L., Akinfiev, N. N., Nickolsky, M. S., Kvashnina, K. O., et al. (2019). Platinum transport in chloride-bearing fluids and melts: Insights from *In Situ* X-ray absorption spectroscopy and thermodynamic modeling. *Geochimica et Cosmochimica Acta* 254, 86–101. doi:10.1016/j.gca.2019.03.023
- Taguchi, K., Zhang, M., Frey, E. C., Xu, J., Segars, W. P., and Tsui, B. M. W. (2007). “Image-domain material decomposition using photon-counting CT,” in Proc. SPIE 6510, Medical Imaging 2007: Physics of Medical Imaging, 651008, San Diego, CA, March 16, 2007 (SPIE). doi:10.1117/12.713508
- Takahashi, T., and Watanabe, S. (2001). Recent progress in CdTe and CdZnTe detectors. *IEEE Trans. Nucl. Sci.* 48, 950–959. doi:10.1109/23.958705
- Tolstykh, N., Brovchenko, V., Rad'ko, V., Shapovalova, M., Abramova, V., and Garcia, J. (2022). Rh, Ir, and Ru Partitioning in the Cu-Poor IPGE Massive Ores, Talnakh Intrusion, Skalisty Mine, Russia. *Minerals* 12, 18. doi:10.3390/min12010018
- Tomkins, A. G. (2010). Wetting facilitates late-stage segregation of precious metal-enriched sulfosalt melt in magmatic sulfide systems. *Geology* 38, 951–954. doi:10.1130/G31263.1
- Van Assche, F., Vanheule, S., Van Hoorebeke, L., and Boone, M. N. (2021). The spectral X-ray imaging data acquisition (Spexidaq) framework. *Sensors* 563, 1–19. doi:10.3390/s21020563
- Voordouw, R. J., Gutzmer, J., and Beukes, N. J. (2010). Zoning of platinum group mineral assemblages in the UG2 chromitite determined through *In Situ* SEM-EDS-based image analysis. *Miner Deposita* 45, 147–159. doi:10.1007/s00126-009-0265-z
- Wang, X., Meier, D., Mikkelsen, S., Maehlum, G. E., Wagenaar, D. J., Tsui, B. M. W., et al. (2011). MicroCT with energy-resolved photon-counting detectors. *Phys. Med. Biol.* 56, 2791–2816. doi:10.1088/0031-9155/56/9/011
- Wirth, R., Reid, D., and Schreiber, A. (2013). Nanometer-sized platinum-group minerals (PGM) in base metal sulfides: New evidence for an orthomagmatic origin of the Merensky Reef PGE ore deposit, Bushveld Complex, South Africa. *Can. Mineral.* 51, 143–155. doi:10.3749/canmin.51.1.143
- Wu, X., Wang, Q., Ma, J., Zhang, W., Li, P., and Fang, Z. (2017). A hyperspectral X-ray computed tomography system for enhanced material identification. *Rev. Scientific Instr.* 88, 083111. doi:10.1063/1.4998991
- Yakubchuk, A., and Nikishin, A. (2004). Noril'sk?Talnakh Cu?Ni?PGE deposits: a revised tectonic model. *Mineralium Deposita* 39, 125–142. doi:10.1007/s00126-003-0373-0
- Yang, B.-h., Wu, A.-x., Miao, X.-x., and Liu, J.-z. (2014). 3D characterization and analysis of pore structure of packed ore particle beds based on computed tomography images. *Trans. Nonferrous Met. Soc. China* 24, 833–838. doi:10.1016/S1003-6326(14)63131-9
- Yang, B., Wu, A.-x., Narsilio, G. A., Miao, X.-x., and Wu, S.-y. (2017). Use of high-resolution X-ray computed tomography and 3D image analysis to quantify mineral dissemination and pore space in oxide copper ore particles. *Int. J. Miner. Metall. Mater.* 24, 965–973. doi:10.1007/s12613-017-1484-4
- Yao, Z., and Mungall, J. E. (2020). Flotation mechanism of sulphide melt on vapour bubbles in partially molten magmatic systems. *Earth Planet. Sci. Lett.* 542, 116298. doi:10.1016/j.epsl.2020.116298
- Yudovskaya, M. A., Kinnaird, J. A., Grobler, D. F., Costin, G., Abramova, V. D., Dunnett, T., et al. (2017). Zonation of Merensky-Style Platinum-Group Element Mineralization in Turfspruit Thick Reef Facies (Northern Limb of the Bushveld Complex)*. *Econ. Geol.* 112, 1333–1365. doi:10.5382/econgeo.2017.4512

Conflict of Interest: Author MB was employed by TESCAN XRE.

The remaining authors declare that the research was conducted in the absence of any commercial or financial relationships that could be construed as a potential conflict of interest.

Publisher's Note: All claims expressed in this article are solely those of the authors and do not necessarily represent those of their affiliated organizations, or those of the publisher, the editors and the reviewers. Any product that may be evaluated in this article, or claim that may be made by its manufacturer, is not guaranteed or endorsed by the publisher.

Copyright © 2022 Sittner, Brovchenko, Siddique, Buysse, Boone, Renno, Cnudde, Merkulova and Sluzhenikin. This is an open-access article distributed under the terms of the Creative Commons Attribution License (CC BY). The use, distribution or reproduction in other forums is permitted, provided the original author(s) and the copyright owner(s) are credited and that the original publication in this journal is cited, in accordance with accepted academic practice. No use, distribution or reproduction is permitted which does not comply with these terms.